
Analysis of Rock Abundance on Lunar Surface from Orbital and Descent Images Using Automatic Rock Detection

Yuan Li, Bo Wu*

Department of Land Surveying and Geo-Informatics, The Hong Kong Polytechnic University, Hung Hom, Kowloon, Hong Kong

* Corresponding author:

Bo Wu, Ph.D.

Associate Professor

Department of Land Surveying and Geo-Informatics

The Hong Kong Polytechnic University

Hung Hom, Kowloon, Hong Kong

Tel: +852 2766 4335

E-mail: bo.wu@polyu.edu.hk

March 2018

This article has been accepted for publication and undergone full peer review but has not been through the copyediting, typesetting, pagination and proofreading process which may lead to differences between this version and the Version of Record. Please cite this article as doi: 10.1029/2017JE005496

Abstract

Information on the distribution and abundance of rocks on the lunar surface is essential for understanding the characteristics of lunar regolith and for selecting suitable landing sites for lunar exploration missions. This paper first presents a novel automatic rock detection approach based on the gradient differences in illumination direction. Multiple-source images covering different regions of the lunar surface are then used for rock detection and rock abundance analysis, including the Chang'E-3 descent images (0.02–0.17 m/pixel) around the landing area, the Lunar Reconnaissance Orbiter (LRO) Narrow Angle Camera (NAC) images (0.3–1.1 m/pixel) at the landing sites of the Chang'E-3, Luna 17, and Luna 23, and the LRO NAC image mosaic (1.5 m/pixel) in the Oceanus Procellarum area. A rock abundance model using an exponential form is derived from the results of the abovementioned analysis to describe the overall cumulative fractional area of rocks versus their diameters. The rock detection results and the derived rock abundance estimated by the proposed model are compared with the ground measurements obtained using the rover images of the Chang'E-3 landing site and the LRO Diviner Radiometer derived rock abundance. A comparison analysis indicates that the derived rock abundance model can feasibly represent the rock abundance in various situations on local and large scales. In general, a remarkable consistency is observed between our results and the results obtained using the ground measurements at the Chang'E-3 landing site and the orbit measurements from the Diviner radiometer, while our rock detection results and rock abundance model exhibit better performance in presenting detailed information in local areas. Further analyses on rock abundance and the crater morphology and other crater characteristics in the Oceanus Procellarum area indicate that it is feasible to use rock abundance information to estimate the surface maturity.

1. Introduction

Lunar regolith records the history of the Moon's interaction with outer space. Studying lunar regolith can enrich our knowledge about the Moon, the Earth-Moon system, and the inner solar system [Crawford and Joy, 2014; Crawford *et al.*, 2014]. As one of the major features exposed on the lunar regolith, rocks have thus always been primary objects of study. For instance, with the successful soft landing of Luna 9, the distribution of rocks on the lunar surface was examined using panoramic photographs [Smith, 1967], which clearly showed a large number of small rocks lying on the surface. The success of a series of NASA's lunar exploration missions, such as the Surveyor and Apollo missions, enabled more in-depth rock distribution analyses at different landing sites on the lunar surface [Cintala and McBride, 1995; Muehlberger *et al.*, 1972; Shoemaker and Morris, 1968]. Recently, the successful landing of the Chinese Chang'E-3 has led to increasing interest in rock size-frequency distribution and the comparison of different landing sites [Basilevsky *et al.*, 2015; Di *et al.*, 2016]. These studies were conducted based on data obtained from the ground and have extended human knowledge about the lunar regolith with close investigations, but they were limited to a small number of local areas around the landing sites on the near-side of the Moon.

To reveal the characteristics of the lunar regolith on a large scale or even for the entire lunar surface, data from the lunar orbiters (e.g., the Lunar Orbiter and the Lunar Reconnaissance Orbiter [LRO]) have been used to investigate the distribution regularity of rocks [Bandfield *et al.*, 2011; Bart and Melosh, 2010; Cintala and McBride, 1995]. However, the size of the rocks that can be recognized from the orbital data is limited by the wavelength of the radar

observation [Thompson *et al.*, 1970], the spatial resolution of the optical images [Cintala and McBride, 1995; Golombek *et al.*, 2003b], and/or the sensitivity of the thermal infrared (TIR) measurements [Bandfield *et al.*, 2011; Nowicki and Christensen, 2007]. As rocks on the planetary surface are potential hazards to the lander or rover, another purpose of previous orbital-data-based studies on rock distributions was to determine suitable landing sites for the planned landing missions [Crawford *et al.*, 2014; De Rosa *et al.*, 2012; Zheng *et al.*, 2008]. This situation is also true for the Mars exploration missions. For instance, one criterion for selecting the landing site of InSight (Interior Exploration using Seismic Investigations, Geodesy and Heat Transport) is that the rock abundance must be less than 10% [Golombek *et al.*, 2017], and for the ExoMars mission is less than 7% [Pajola *et al.*, 2014].

Given these circumstances, a rock abundance model that describes the relationship between the cumulative fractional area covered by rocks and the rock diameter is needed to estimate the overall area covered by rocks. In practice, a rock abundance model can be formulated based on large rocks that can be recognized from the relatively low-resolution orbital observations, incorporating the small rocks identified from high-resolution ground data or other types of images of the local regions. Golombek and Rapp [1997] proposed a rock abundance model for Mars based on the data collected at the Viking 1 and 2 landing sites, and the model was then tested and constrained using the Mars Orbiter Camera (MOC) and High Resolution Imaging Science Experiment (HiRISE) images [Arvidson *et al.*, 2008; Golombek *et al.*, 2008; Golombek *et al.*, 2003b]. The rock abundance model has been widely used for selecting the Mars mission landing sites [Arvidson *et al.*, 2008; Golombek *et al.*, 2012a; Golombek *et al.*, 2003a; Golombek *et al.*, 2017]. In the study of Golombek *et al.* [2017], it is also found that rock abundance model can be used to estimate the negative binomial process of the regolith formation. To the best of our knowledge, although some

efforts have been made to analyze the rock distributions at several landing sites on the Moon [Cintala and McBride, 1995; Di et al., 2016; Shoemaker and Morris, 1968], no such rock abundance model or comprehensive analysis is currently available for the Moon.

This paper presents a rock abundance model of the lunar surface by combining the rock size-frequency analyses derived from multiple-source imagery, including the high-resolution LRO NAC images, descent images acquired around the Chang'E-3 landing site, and ground observations at the Chang'E-3 landing site. For this purpose, a novel rock detection approach is developed to automatically identify rocks from the optical images. Comparisons with published data from different sources are made to verify the proposed rock detection approach and the rock abundance model. Further analyses are also carried out to investigate the relationships between rock abundance and surface maturity by means of crater morphology and other crater characteristics.

2. Literature Review

Mars and the Moon have similarities in terms of geophysical characteristics because they both lack a substantial atmosphere. The technologies, observation methods, and data used for exploring Mars and the Moon are also similar. In addition, the purposes of rock distribution studies on Mars and the Moon are similar — to understand the geological properties and to select suitable landing sites for exploration. Therefore, related research on rock abundance on Mars can be a valuable reference for that on the Moon. Hence, this paper first presents a review of rock abundance-related research on Mars.

2.1 Rock Abundance on Mars

To map the global rock abundance on the Martian surface, Christensen [1986] developed a rock abundance model based on the temperature contrasts between rocks and the fine components related to the thermal emission differences in the four spectral bands of the Viking Infrared Thermal Mapper observations. Based on similar theories, thermal emission data from the Mars Global Surveyor Thermal Emission Spectrometer were also used to generate global rock abundance and fine-component inertia maps [*Mellon et al.*, 2000; *Nowicki and Christensen*, 2007]. These studies benefitted from the large coverage of the orbital data and provided important clues for selecting the landing sites for the Mars Pathfinder (MPF) [*Golombek et al.*, 1997] and other Mars missions. However, the resolution of the products was very low (e.g., 1 pixel/degree [*Christensen*, 1986] and 8 pixel/degree [*Nowicki and Christensen*, 2007]), and only general observations can be derived from these products. In addition, observations related to thermal emissions are likely to be affected by the presence of water-ice and atmospheric dust [*Christensen*, 1986], which will consequently lead to an uncertainty in rock abundance and the inability to make estimates at high latitudes [*Nowicki and Christensen*, 2007].

Another important data source for rock studies on Mars is the ground images obtained by the cameras onboard the landers or rovers. A number of studies have been conducted to analyze the size-frequency distribution and rock abundance based on such images since the two successful Viking missions [*Golombek and Rapp*, 1997; *Moore and Keller*, 1991; *Moore et al.*, 1987]. Using stereometric measurements and contour maps, *Moore and Keller* [1991] mapped more than 400 rocks larger than 0.1 m diameter located in front of the two Viking

landers. Later, based on these data as well as data collected at a number of Earth analog sites, Golombek and Rapp [1997] suggested that an exponential function, which shows convex-up curves on a log-log graph, should be used to model the cumulative fractional area covered by rocks versus diameter according to the fracture and fragmentation theory [Gilvarry, 1961; Gilvarry and Bergstrom, 1961]. This exponential model was later tested with the rock fields observed by the MPF [Golombek *et al.*, 2003b], and the results for the MPF landing site were consistent with those for the Viking 2 landing site. Golombek *et al.* [2005] investigated the rock size-frequency distributions at multiple sites along the Spirit rover traverse across the Gusev cratered plains, using Pancam and Navcam images and panoramas. The results indicated that the exponential model is generally followed by the rock size-frequency distribution curves of these sites.

Remotely acquired optical images collected from the orbiters are also a very important data source for rock studies. In Golombek *et al.* [2003b], more than 14,000 rocks with diameters of larger than ~5 m were measured from six MOC images (~3 m/pixel). Despite the fact that the size-frequency distributions of rocks derived from the MOC images were considerably higher than those estimated by the rock abundance model [Golombek and Rapp, 1997], the shapes of the distributions were parallel to the model distribution, which showed a steep reduction with an increase in the diameter. For selecting the Phoenix landing site, Golombek *et al.* [2008] proposed a shadow-based rock detection method, which separates rock shadows from the background terrain by applying a modified maximum entropy thresholding algorithm [Huertas *et al.*, 2006], and then identifies the locations and shapes of rocks based on the detected shadows. Using this method, hundreds of thousands of rocks were counted from the HiRISE images (~0.3 m/pixel). The size-frequency distribution of these rocks was consistent with that of manually identified rocks [Arvidson *et al.*, 2008]. A further

comparison with previous studies [Golombek and Rapp, 1997; Golombek *et al.*, 2003b] suggested that the distribution patterns of rocks with a diameter of greater than 1.5 m derived from the HiRISE images coincided with the distribution of smaller rocks derived from ground observations at the landing sites, which also indicated the effectiveness of the exponential rock abundance model proposed by Golombek and Rapp [1997]. After the landing of Phoenix, Heet *et al.* [2009] examined the distribution of rocks larger than 5 cm from the Surface Stereo Imager (SSI) images, which covered a region of 70 m² around the Phoenix lander, and later Golombek *et al.* [2012b] expanded the investigation to 176 m² around the lander, where 27 large rocks (0.13 – 0.4 m in diameter) were identified. The cumulative fractional area versus diameter of these surface-measured rocks was compared with the result counted on HiRISE images. The comparison revealed that the size-frequency distributions of both the surface-measured rocks and orbital image-measured rocks generally follow the exponential model with rock abundances of 2-4% and 3-4%, respectively [Golombek *et al.*, 2012b]. Golombek *et al.* [2017] also used this technique to measure rocks at the InSight landing site using HiRISE images, and showed that there is a considerable consistency between the exponential rock abundance model and the fragmentation from impacts estimated from the cratering record, which could be fitted by a negative binomial function.

In summary, orbit thermal emission data, ground images collected by landers or rovers, and orbit optical images are the three main data sources for rock abundance analysis on Mars. Orbit thermal infrared data can provide large coverage, however, the resolutions of the products are low. Ground images enable detailed and accurate rock measurements, which lead to the widely accepted exponential model of rock abundance on Mars. However, ground images only provide small segmented coverages. It is desirable to link them to descent or

orbit images to verify the rock abundance in large scales. Measurements from the orbit optical images can cover a large area. However, only relatively large rocks can be detected dependent on the resolution of the images, which may result in the rock size-frequency distribution deviated from the ground measurements. Therefore, integration of multiple-source (ground, descent, and orbit) images with high resolutions for rock abundance analysis has the potential to generate more reliable results.

2.2 Rock Abundance on Lunar Surface

TIR measurements of the Moon began with Earth-based telescopic observations in the 1920s [Shorthill, 1970], but these super-remote observations failed to provide detailed information of the lunar surface. In the 1970s, some short-term *in situ* heat-flow experiments were conducted to measure the thermal conductivity of lunar surface materials during the Apollo 15 and 17 missions at the Hadley Rille and Taurus-Littrow sites, respectively [Grott *et al.*, 2010; Keihm and Langseth Jr, 1973; Langseth *et al.*, 1976], making it possible to distinguish rocks from the regolith fines on the basis of the high contrast between their thermal conductivities [Roelof, 1968]. However, such measurements are only limited to some local sites. The Apollo 17 mission also measured the thermal emission of the lunar surface using an infrared scanning radiometer onboard the orbiter [Mendell and Low, 1974]. Although the Apollo 17 radiometer data covered large areas, the data were not multi-spectral preventing a robust derivation of rock abundance. Bandfield *et al.* [2011] extended this research to an almost global scale by using the measurements from the LRO Diviner radiometer. The relationships between the regolith temperatures derived from the thermal emission measurements and the concentration of lunar rocks, which were assumed to have temperature

properties similar to those of the vesicular basalt, were modeled based on Planck's radiance law. The results from this study was a rock concentration map covering all longitudes and latitudes ranging from 60°N to 60°S with a resolution of 32 pixel/degree, showing that the average fractional area covered by rocks within this range was 0.4%. The latest product released on the PDS Geosciences Node (<http://ode.rsl.wustl.edu/moon/index.aspx>) extended the latitude coverage to 80°N ~ 80°S, with a resolution of 128 pixel/degree, which is used for comparison analysis in this paper. However, according to the manual comparison between the rock concentration derived from the Diviner data and that derived from the LRO NAC images [Bandfield *et al.*, 2011], the Diviner results were likely to present only the fractional area covered by rocks with diameters larger than 1 m.

A number of studies in the past investigated the physiographic characteristics near the landing sites. For instance, on the basis of the photographs collected by Luna 9, which achieved the first successful soft landing on the Moon, Smith [1967] stereoscopically measured more than 100 rocks ranging from 2 to 24 cm in diameter and modeled the rock density versus diameter with a power function. Later, with the success of the Surveyor missions, Shoemaker and Morris [1968] studied the rock size-frequency distribution using images at the Surveyor landing site and used a power function to describe the population of rocks larger than 10 cm in diameter. The rock distributions at the landing sites of the Apollo 11 and 16 were also studied based on the panoramic images composed of the photographs taken by the astronauts [Aldrin Jr *et al.*, 1969; Muehlberger *et al.*, 1972]. More recently, Di *et al.* [2016] identified 582 rocks smaller than 1 m in diameter using the Navcam stereo images taken by the Chang'E-3 Yutu rover, via interactive measurement. The detected rocks were then used for the rock distribution and size-frequency analyses, and the results suggested that

the cumulative fractional area of rocks versus diameter was fitted well by exponential curves, which was similar to those at the landing sites on Mars [Golombek *et al.*, 2005; Golombek *et al.*, 2012b; Golombek *et al.*, 2008; Golombek and Rapp, 1997; Golombek *et al.*, 2006; Golombek *et al.*, 2003b; Heet *et al.*, 2009].

In addition to the abovementioned studies based on TIR observations or optical images collected at landing sites, orbiter images (e.g., the Lunar Orbiter and LRO NAC images) have also been used for the measurement and analysis of rock size-frequency distribution on relatively larger scales. However, only a few studies have used such images, and they were only as supplements to other methods. For instance, to further understand the geological characteristics of the four Surveyor (I, III, VI, and VII) landing sites, large rocks (i.e., larger than 2.5 m in diameter) in the vicinity were derived from the Lunar Orbiter images and compared with those from the Surveyor images [Cintala and McBride, 1995]. In Bandfield *et al.* [2011], manually counted rocks from the LRO NAC images were used to verify the rock concentration derived from the LRO Diviner data. Other research treated the rock distribution as an important factor for safe landing and landing site selection and thus studied the rock distributions in the potential landing areas using the LRO NAC image mosaics [De Rosa *et al.*, 2012].

Although the aforementioned studies have, to some degree, enriched our knowledge of rock distribution on the lunar surface, there is still a gap between rock abundance analyses at landing sites and the comprehensive analysis of rock distribution on a large scale or even for the entire Moon, for the following reasons. (1) Rock abundance studies based on ground data [Di *et al.*, 2016; Shoemaker and Morris, 1968; Smith, 1967] can identify small rocks (~0.1 m

in diameter). The cumulative areal fraction of rocks is believed to be equal to the overall rock abundance, but obviously, these studies have failed to extend the investigations to a larger scale beyond the landing sites. (2) Existing mapping products from the Diviner data [Bandfield *et al.*, 2011] provide a direct presentation of the rock concentration on an almost global scale, but the results only refer to the fractional area covered by rocks larger than approximately 1 m in diameter, and no detailed information (e.g., areal fractions of rocks with different diameter ranges) can be obtained. (3) High-resolution optical images such as the LRO NAC images can intuitively present the distribution and physical properties (e.g., size and shape) of the rocks exposed on the lunar surface, but few studies have been conducted to fully take advantage of such data and integrate the results with data from other sources. This paper is an attempt to bridge that gap by developing a rock abundance model covering all ranges of rock sizes, from which the overall rock abundance at any spot on the lunar surface can be estimated using rock distributions derived from high-resolution orbit images. For this purpose, an automatic rock detection approach is first developed for the identification of rocks from images.

3. A Novel Automatic Rock Detection Approach

3.1 Overview of the Approach

Rock detection and measurement are the basic requirements of rock size-frequency and abundance analyses. However, in related rock studies based on images [Bandfield *et al.*, 2011; Cintala and McBride, 1995; De Rosa *et al.*, 2012], rock detection has usually been accomplished manually, which can be extremely time-consuming due to the small size and

large number of rocks existing on the lunar surface. Therefore, to achieve fast rock detection on a large scale with more automation, this paper presents an automatic rock detection approach based on the gradient differences along the illumination direction in the optical images. The fundamental idea is that, due to the relief of ground features (e.g., rocks and craters), the incident angles of sunlight vary with the surface fluctuation. Therefore, when the ground features are imaged in the images, their brightness distributions are different. Figure 1 illustrates the imaging of terrain features and the brightness differences in the images. It should be noted that the actual brightness distribution could be complicated due to terrain relief and albedo variations, but in general, image pixels corresponding to rocks and the sunward side of craters have brighter intensities than surround terrains.

Accepted Article

The framework of the rock detection approach is illustrated in Figure 2. First, the illumination directions at the time of image acquisition are determined. As image mosaics are generated from images with different illumination directions, the images are split into different segments, each of which has a unified illumination direction. Then, the regions of interest (ROIs) are selected before rock detection to improve the detection performance. Finally, the rocks in each ROI are detected and output as fitted ellipses with geometric and positional information. The following sub-sections describe each step in detail.

3.2 Extraction of Illumination Directions

Ground features (mainly craters and rocks) shown in the images are generally presented as a set of bright and dark pixels with different distributions. The brightness distribution of pixels is directly related to the illumination direction, which changes with the time and place of image capture. In this research, illumination direction is identified based on the fact that the sunward side of a crater is bright, whereas the downsun side is in shadow (see Figure 3), and this estimated illumination direction is further confirmed by sun illumination information recorded in the image labels if the label information is available. We compared the estimated illumination directions of three LRO NAC images (M1116664800, M175502049, and M174868307) with the solar azimuth angles computed based on the image label information, and the results indicate that the deviations are less than 3.5° (details can be referred to the image information described in Section 3.6). In consideration of the discrete property of the image, the estimated illumination direction can present the distribution relation between rock pixels and rock shadows with this small deviation when no label information is available. Generally, one image corresponds to only one illumination direction. However, for image

mosaics, there can be multiple illumination directions as shown in Figure 3. In this case, the different illumination directions are determined interactively and the image mosaic is split into different segments, each of which corresponds to a unified illumination direction.

3.3 Selection of ROIs

As most lunar surfaces are nearly rock-free [Bandfield *et al.*, 2011] and small rocks (within 2 pixels on the image) cannot be clearly recognized from the images, regions where rocks are likely to be shown on the images, namely regions of interest (ROIs), are firstly selected by merging the bounding boxes of edges detected by the Canny algorithm [Canny, 1986]. And the rock detection will only be performed within the ROIs so that the efficiency of the approach can be improved. In fact, edge information has been widely used for feature detection using images [Thompson and Castano, 2007]. However, edge information cannot be directly used for rock identification as edges are irregular and complicated polylines as shown in Figure 4(b), which makes it difficult to distinguish rock edges from other edges in an image. Nevertheless, edge detection can provide important clues for predicting regions where rocks may exist. Therefore, we developed a ROI selection approach based on edge information, as illustrated in Figure 4. Firstly, edges (Figure 4(b)) of ground features, including rocks, craters, and shadows cast by rocks, are firstly detected using the Canny algorithm with a 3×3 Sobel kernel [Gao *et al.*, 2010] (as shown in Equation (1)) from the original image (Figure 4(a)). The Canny algorithm is selected because it has shown favorable performances even under noise conditions [Sharifi *et al.*, 2002]. These detected edges are then fitted by the minimum bounding rectangles (green rectangles in Figure 4(c)), and finally,

the ROIs (yellow rectangles in Figure 4(d)) are formed by iteratively merging the overlapping bounding rectangles (green rectangles in Figure 4(c)) until no rectangles are overlapped.

$$G_x = \begin{bmatrix} -1 & 0 & +1 \\ -2 & 0 & +2 \\ -1 & 0 & +1 \end{bmatrix}, \quad G_y = \begin{bmatrix} -1 & -2 & -1 \\ 0 & 0 & 0 \\ +1 & +2 & +1 \end{bmatrix} \quad (1)$$

3.4 Rock Detection

Referring to the rock and crater examples in the images of the lunar surface, the pixel intensities (all the images used in this paper are converted into 8-bit format and the values of pixel intensity range from 0 to 255) can be roughly grouped into three categories: bright (sunward side of the rock or crater), medium (flat ground), and dark (shadow). The gray differences among them can be generalized as

$$\begin{cases} p_{bright} - p_{medium} = d \\ p_{medium} - p_{dark} = d \end{cases} \quad (2)$$

where p_{bright} , p_{medium} , and p_{dark} refer to pixels with different gray values, and d is the approximate brightness differences between them.

For each pixel p , two gradients g_1 and g_2 are calculated, where g_1 is the gradient along the light direction and g_2 is the gradient opposite the light direction. Let $G_1 = g_1 + g_2$ and $G_2 = g_1 - g_2$. Theoretically, G_1 and G_2 show different values when p moves on the image. Assuming that the illumination direction is from left to right, Table 1 shows the most likely brightness distribution cases.

According to Table 1, both G_1 and G_2 are prone to large values ($\geq d$) when the processing window moves on rock pixels, especially for small rocks (1 or 2 pixels). Some small terrain relief or surface albedo variations may show similar brightness distribution pattern with rocks, but their intensities are not as high as rocks, which means they have smaller G_1 and G_2 values. Therefore, with appropriate thresholds τ_1 and τ_2 (τ_1 and τ_2 are determined by selecting samples of bright pixels, medium gray pixels and dark pixels corresponding to rocks, regolith, and shadows, and computing the gradients between the average values of the samples, and they are generally set as 60 and 20, respectively) small rocks can be detected by judging whether the values of G_1 and G_2 are greater than thresholds τ_1 and τ_2 . Table 1 also lists two cases of brightness distribution of large rocks (3 or more pixels). One is a large rock contains only bright pixels and another is a large rock contains bright and gray pixels, which is possibly caused by the convexity of the rock top and high solar incident angle. A pyramiding strategy is adopted to measure rocks of varying sizes.

An image pyramid is a set of images, all of which are derived from a single image by successively down-sampling, and each image in the pyramid is called a layer. Figure 5 shows two examples of large rocks. In the image pyramid, layer 0 has the same resolution with the original image, and each higher layer is 2-to-1 down-sampled from the lower layer. For each layer, rock pixels are detected based on the principle described previously, and the results are shown in the second row in Figure 5 (a) and (b). It is shown that large rocks on pyramid layer 0 are only partly detected. This is because the above principle assumes that rocks are small objects occupying only ~2 pixels in illumination direction, and therefore for large rocks, only the pixels near the shadow are detected. But in higher layers, rocks can be gradually detected

completely as they are down-sampled to smaller sizes (as shown in pyramid layer 1 and layer 2 in Figure 5). Gray pixels belonging to a rock can also be detected from higher pyramid layers (as shown in Figure 5(b)), because the interpolation process when generating pyramids introduces neighboring information to the detection. All the rock pixels detected from each pyramid layer are then merged to the original image as shown in the last column of Figure 5. To reduce the inaccuracy of rock boundaries caused by down-sampling, pixels with very low brightness on the original image are excluded during the merging stage. The merged rock pixels are finally clustered using an eight-neighborhood clustering algorithm and output as ellipses representing rock boundaries.

Figure 6 shows the overall procedure of rock detection in an ROI, where the rock size varies significantly. Each pyramid layer is down-sampled to the higher layer while layer 0 is the ROI cut from the original image. It can be seen that the small rocks are correctly detected on layer 0 as shown in Figure 6 (a), and large rocks (marked with white circles) are detected via the process illustrated in Figure 5. All the detected rock pixels are merged to the original image (Figure 6(b)) and then clustered and fitted with ellipses (Figure 6(c)), of which the longer diameters determine the diameters of rocks.

3.5 Filtering of False Detections

There could be two reasons for false detections occurring around craters (as shown in Figure 7(c)) when the method described above is used. First, the rim of a crater may have the same convexity as that of a rock and consequently have the same brightness distribution. This will directly lead to a false detection around the crater's rim on the light incidence side of the

crater. Second, the gray level from the light incidence side to the exit side of a crater changes smoothly from dark to bright. Because of the pyramiding strategy, a transition may coincidentally make the brightness distribution at the light exit side of the crater looks like a rock. False detections could also exist at certain places where small terrain relief exists. The convexity of the terrain relief might make their brightness distribution similar to rocks along the illumination direction, especially when the terrain relief has linear shapes perpendicular to the illumination direction (see in Figure 7(d) for example), which will consequently cause false detections.

Based on the fact that the neighboring pixels of true detections (rocks) and false detections (craters and small terrain relief) have different brightness distributions along the perpendicular direction of illumination, a filtering process is carried out to exclude the false detections on the basis of seeded region growing [Adams and Bischof, 1994]. Taking the rock pixels detected by our approach (marked with pink in Figure 7) as seeds, the neighboring pixels are iteratively included into the region if they have similar brightness values, and the new pixels (marked with blue in Figure 7) obtained through region growing are defined as “grown pixels”. As shown in Figure 7, for true detections (Figure 7(a) and (b)), the clusters of initially detected pixels (in pink) barely grows, but for false detections, the clusters of grown pixels (in blue) are considerably larger than the initially detected clusters. Hence, the false detections can be excluded by judging whether the difference between the cluster of grown pixels and the cluster of detected pixels is greater than a given threshold τ_3 , and τ_3 is set as 15 in this research based on our extensive experimental observations that the grown size of true detections is rarely larger than this value, while the false detections will grow extremely larger.

3.6 Rock Detection Results and Evaluation

We used images from different sources for rock detection and rock abundance analysis, including (1) geo-referenced descent images (0.02-0.17 m/pixel) around the Chang'E-3 landing area (19.51°W , 44.12°N) [Wu *et al.*, 2014], (2) high-resolution LRO NAC images (0.3-1.1 m/pixel) covering the landing sites of the Chang'E-3, Luna 17 (35°W , 38.24°W), and Luna 23(62.15°E , 12.67°N), and (3) LRO NAC image mosaic with a relatively low resolution (1.5 m/pixel) and covering an area of $182 \times 166 \text{ km}^2$ ($55 \sim 49^{\circ}\text{W}$, $41 \sim 45^{\circ}\text{N}$) in the Oceanus Procellarum, which belongs to a part of the candidate landing area of Chang'E-5 [Zhao *et al.*, 2017].

The descent images were collected by the descent camera (Descam) mounted on the bottom of the Chang'E-3 lander and facing downward with a nominal field of view (FOV) of 45.4° , and a nominal focal length of 8.3 mm. The Chang'E-3 Descam acquired 4672 images each with a size of 1024×1024 pixels during the descending phase from a height of 2 km to the ground [Liu *et al.*, 2015]. In this study, 18 descent images from the hovering stage to the touchdown stage were selected to generate an orthographic image mosaic, which was then geo-referenced to the LRO NAC image (1.1 m/pixel), as shown in Figure 8(a) and (b), respectively. The orthographic descent image mosaic covers an area of $13,100 \text{ m}^2$ and has an irregular shape due to the occlusions caused by the Descam holder. The spatial resolution of the generated descent image mosaic ranges from 0.02 m/pixel to 0.17 m/pixel from the center to the boundary, as the central parts correspond to the descent images closer to the ground and thus, have better spatial resolution. The Chang'E-3 landing site is marked with a white cross in Figure 8(b) for reference.

The high-resolution LRO NAC image (M1116664800) covering the Chang'E-3 landing site is also exploited in this study for a comparison with the descent images. The selected region contains two large craters (>400 m in diameter) named Zi Wei (C1) crater and Tai Wei crater (see in Figure 8(a)), where most of the rocks are located. In addition, the LRO NAC images (M174868307 and M175502049) at the two landing sites of Luna 23 and 17 are used for analysis as they have very high resolutions of 0.3 m/pixel and 0.35 m/pixel, respectively. They are shown in Figure 8(c) and (d). The image mosaic generated from multiple LRO NAC images covers an area of 30,212 km² on the western edge of Oceanus Procellarum, as shown in Figure 8(e), which is a larger area where the terrain surface varies with not only the distribution of the craters but also the appearance of other features such as a lava flow. The lava flow has a length of about 140 km in the study area and the slopes of its two sides range from 4.3° to 7.1°. The detailed parameters of the LRO NAC images and the NAC mosaic are given in Table 2. The solar azimuth angle is computed based on the sub solar longitude/latitude and the center longitude/latitude of the image. Note that, the LRO NAC mosaic is generated from multiple NAC images, therefore no unique solar incidence angle or phase angle can be obtained.

The proposed approach is used for automatic rock detection from the multiple-source images described above. For further analyses, some sub-areas are selected from the Chang'E-3 landing area including two rectangle areas containing Zi Wei (C1) crater (19.52°W, 44.12°N) and Tai Wei crater (19.50°W, 44.15°N) in the LRO NAC image (see Figure 8(a)), and a circular area around the C2 crater and the traverse area of the Yutu rover on the Chang'E-3 decent image mosaic (see Figure 8(b)). The latter is the same as the study area in Di *et al.* [2016], for a comparison and correlation analysis with the results from Di *et al.* [2016]. The

final detected rocks are overlaid on the corresponding images as shown in Figure 8, from which it can be seen that most of the detected rocks are distributed around impact craters with a radial pattern, and some rocks are located on the slopes of the lava flow (see Figure 8(e)).

Detailed information on the rocks detected is presented in Table 3, where the diameter refers to the long diameter of the fitted ellipse.

Accepted Article

To quantitatively evaluate the reliability of the proposed rock detection approach, the rocks automatically detected by our approach in four local regions, which are marked with 1-4 in the Oceanus Procellarum area (see Figure 8(e)), are compared with the manual digitization results within the same four regions. These four regions were selected because of their different geological characteristics. The manual digitization was performed using the software ArcGIS 10.2. In this software, rocks shown on the image covering minimum 2 pixels in diameter are manually fitted by ellipses. The purpose of the evaluation is to find out how completely and correctly the proposed approach can detect rocks that can be recognized on the images. Therefore, the manual digitization results are regarded as “ground truth”, and a benchmark based on this “ground truth” is performed. Let A_1 be the total area covered by the automatically detected rocks from the proposed approach and A_2 be the total area of the manually digitized rocks. A_3 is the overlapping between A_1 and A_2 indicating the area covered by true positive rocks. The correctness and completeness of rock detection are defined as

$$\begin{cases} \text{correctness} = A_3 / A_1 \\ \text{completeness} = A_3 / A_2 \end{cases} \quad (3)$$

The correctness measures the percentage of the true positive detections in the automatically detected results, and completeness measures the percentage of true positive detections in the manually detected results (ground truth). The detailed results are shown in Table 4 and Figure 9.

Table 4 shows that the average correctness and completeness of rock detection for the four regions are 88.61% and 80.06%, respectively. The correctness is higher than the completeness in each region, which implies that some rocks are omitted during the automatic detection process. Note that most of the omitted rocks are located in regions with poor image

quality, as shown in Figure 10(b), where the low brightness contrast between rock pixels and the surrounding pixels makes it difficult to distinguish the rocks from the background. High contrast brightness as shown in Figure 10(a) is thus preferred for the proposed approach.

With respect to the correctness, there could be two major reasons for the false positive detections. First, two clusters of bright pixels that are very close to each other (see the example in Figure 10(a)), tend to be treated as one large rock by our approach, while they are manually digitized as two rocks, and this will cause false positive results in the benchmark. Second, during filtering false detections near craters, the size of the grown pixels (the blue pixels shown in Figure 10(c)) is related to the size of the crater, and this may lead to some false detections around the boundaries of very small craters that escaped filtering.

To further improve the correctness and completeness of the automatically detected rocks, a manual checking process – deleting false positive detections and adding omitted rocks — is carried out subsequently. In practice, considering that manual deleting is more efficient than manual adding, the thresholds (τ_1 , τ_2 , and τ_3) are adjusted based on the image brightness to increase the number of true positive detections while allowing relatively more false positive detections. Overall, the proposed approach can shorten the time of manual work by about ten times, indicating the promising performance of the proposed approach.

4. Rock Abundance Analysis

4.1 Rock Abundance Model

Rock abundance refers to the total area covered by all the rocks in a unit area. However, due to the limitations of the image resolution, the measurement of rocks of all sizes is difficult. A common way to estimate the rock abundance on the lunar surface, as well as on Mars, is to analyze the cumulative fractional area of rocks versus their diameter, which is always shown as convex-up curves on a log-log graph [Di *et al.*, 2016; Golombek *et al.*, 2008; Golombek and Rapp, 1997; Golombek *et al.*, 2003b]. The cumulative fractional area versus diameter analysis of the previous rock detection results in this research is shown in Figure 11, of which the diameters of rocks are determined by the longer diameters of the corresponding ellipses.

Similar to the rock abundance study on Mars [Golombek *et al.*, 2012a; Golombek *et al.*, 2008; Golombek and Rapp, 1997; Golombek *et al.*, 2003b], here, the curves can be fitted by an exponential curve with the following form:

$$F_k(D) = ke^{-qD} \quad (4)$$

where k is the overall rock abundance, $F_k(D)$ refers to the areal fraction of rocks larger than D in diameter, and q is the exponential coefficient.

The values of k and q , as well as the R^2 value of the least squares fitting of each exponential curve, are given in Table 5.

According to Golombek and Rapp [1997], there is a negative correlation between k and q :

$$q(k) = A + B/k \quad (5)$$

where A and B are two constant coefficients. This function is adopted in our research as well.

Based on the fact that higher image resolution leads to more accurate detection results, which has been suggested by similar studies on Mars [Golombek et al., 2012b; Golombek et al., 2008; Golombek et al., 2017; Golombek et al., 2003b], only the first five datasets (image resolutions are all better than 0.5 m/pixel) in Table 5 are used to determine the coefficients A and B . The values of A and B in the rock abundance model are determined to be 0.5648 and 0.01285, respectively, and with a R^2 of 0.96. Therefore, the rock abundance model derived from this research is given as:

$$F_k(D) = ke^{-(0.5648+0.01285/k)D} \quad (6)$$

It should be noted that, although the above rock abundance model is derived from the five available high-resolution datasets, it can be used or referred to estimate the rock abundance at any other place on the lunar surface. Similar strategies have been used for rock abundance analysis on Mars [Golombek et al., 2008; Golombek et al., 2003b].

The comparison between the curves generated from the detected results and the curves obtained using the abovementioned rock abundance model (with different rock abundance values) is shown in Figure 12. In general, the landing areas of Chang'E-3, Luna 17, and Luna 23 have a low rock abundance of less than 1.5%. The rock abundance values in the Yutu traverse area and the area covered by the Chang'E-3 descent images range from 1% to 1.2% and are very close. The Luna 23 landing area has the lowest rock abundance of approximately

0.9%, and the rock abundance in the Luna 17 landing area (Lunokhod 1 traverse area) is relatively high because it contains a part of a large crater. C2 crater, Zi Wei (C1) crater and Tai Wei crater are all close to the Chang'E-3 landing site and have similar rock abundances of around 6%. Further, the continuity between C2 crater (from descent images with a resolution of 0.1 m/pixel) and Zi Wei (C1) crater and Tai Wei crater (from the LRO NAC image with a resolution of 1.1 m/pixel) is well fitted by our model (see the red line with diamond symbols and the black lines with triangle and square symbols), which indicates that our rock abundance model can correctly estimate the rock abundance with a specified diameter based on the observations.

In contrast, the rock size-frequency distributions of regions 1-4 (from the LRO NAC image mosaic with a resolution of 1.5 m/pixel) have higher values than the model curves with an increase in the diameter; these results are in agreement with similar studies on Mars [Golombek *et al.*, 2008; Golombek *et al.*, 2003b]. There are two major reasons for the differences between the rock size-frequency and model curves. First, the boundaries of the rocks are ambiguously identified because of the discrete properties of the image data, and the lower the image resolution is, the larger the deviation from the real rock boundaries is. Second, as illustrated in Figure 13, a cluster of small rocks is likely to be identified as one large rock in a relatively low-resolution image, which results in a higher fractional area of large rocks being derived from the low-resolution image than in reality, and this deviation increases with an increase in the rock diameter.

4.2 Comparison with Observations from Rover Images at the Chang'E-3 Landing Site

The rock size-frequency distribution at the Chang'E-3 landing site was also investigated by Di *et al.* [2016] using the ground images (1024×1024 pixels with 0.27 mrad per pixel) collected by the Navcam onboard the Yutu rover, which cover the same region as the Yutu traverse area in this research. The Navcam has a FOV of 46.4° and a focal length of 17.7 mm. A comparison of our results derived from the descent images and the results obtained from the Yutu rover images by Di *et al.* [2016] is shown in Figure 14 and Figure 15. The rover images cover seven waypoints (numbered as N0101, ..., N0107). In total 582 rocks were manually measured by Di *et al.* [2016] from the rover images collected in these seven waypoints as shown in Figure 14(a). As the resolutions of the descent images used in this research are lower than the Yutu rover images, fewer rocks with a total number of 378 are detected from exactly the same region (as shown in Figure 14(b)). According to Di *et al.* [2016], the rock with the maximum diameter of 1.533 m appears at waypoint N0101, which is the closest to the C2 crater as shown Figure 14(a). And the largest rock measured by our approach from the descent image also appears around the rim of C2 crater with a diameter of 1.65 m, which indicates they are highly likely to be the same rock. The difference between the diameters is less than 0.12 m, and considering the resolution of the descent image covering this area is 0.06 m/pixel, the deviation of the diameters is less than 2 pixels.

Exponential curves (black curves shown in Figure 15) from Di *et al.* [2016] are fitted based on the measurements at each waypoint and for the entire region. By comparing our rock size-frequency curve (the one with red triangle symbols in Figure 15) with the fitted curve of all the waypoints obtained by Di *et al.* [2016] (the one with black triangle symbols in Figure 15), we find that with rock diameter getting smaller, our curve derived from the descent images is slightly lower than the curve derived from the rover data. This difference can be attributed to the facts that the resolution of the descent images ranges from 0.02 to 0.13 m/pixel in this

area and that rocks smaller than approximately 0.3 m (the minimum rock size that can be recognized from the descent images at the lowest resolution) are inevitably undercounted.

However, generally a good consistency is observed between these two curves, which

indicates the reliability of our rock detection results.

With respect to our rock abundance model, the fitted curve corresponding to all the waypoints also conforms to the model curve with $k = 1.15\%$, as does the rock size-frequency distribution derived from the descent images. For the fitted curves corresponding to different waypoints, however, the model curves are not quite well followed. The reason may be that the study area is very small and the total number of rocks counted at each waypoint is less than 100 except for waypoint N0101 [Di *et al.*, 2016], and small-scale studies are prone to be affected by random factors.

4.3 Comparison with LRO Diviner Radiometer Data

The lunar global rock abundance map generated from the LRO Diviner radiometer data using the method of Bandfield *et al.* [2011] is used for comparing with our rock detection results and verifying the validity of our rock abundance model. The Diviner global map has a resolution of 128 pixel/degree (approximately 237 m/pixel at the equator) and a coverage of all longitudes and $80^{\circ}\text{N} \sim 80^{\circ}\text{S}$. According to the comparison with the rock size–frequency distribution derived from the LRO NAC images [Bandfield *et al.*, 2011], each Diviner bin represents the areal fraction of rocks larger than approximately 1 m in diameter.

4.3.1 Comparison in Local Representative Regions

Figure 16 shows the Diviner rock abundance map overlaid on our rock detection results for eight local regions (blue stands for 0 rock abundance and red for 25% rock abundance, which approximates the maximum rock abundance value in these eight local regions). The Diviner rock abundance map shows qualitative agreement with our rock detection results in regions 1-4 (on the LRO NAC image mosaic with a resolution of 1.5 m/pixel) as can be seen in Figure 14(e)-(h). In contrast, the comparison in relatively smaller regions (Figure 16(a)-(d)) does not provide sufficient support to state that the Diviner rock abundance map is consistent with our results. This finding suggests that the Diviner rock abundance map may not be able to accurately describe the rock abundance information in local small regions.

A quantitative comparison of the rock size-frequency distributions, model-fitted values, and the Diviner data is presented in Table 6. The first row in the table presents the k values (rock abundances) obtained by fitting the corresponding rock size-frequency curves (see Figure 12) with our rock abundance model. Note that as the rock size-frequency curves of regions 1-4 do not follow the rock abundance model, the corresponding k values are determined on the basis of the fractional area of rocks larger than 3.0 m (the minimum size that can be recognized from a 1.5-m/pixel image). This finding can be attributed to the fact that in low-resolution images, the cumulative fractional area of small rocks is closer to the reality than that of large rocks (refer to the discussion in Section 4.1). All the other values in Table 6 refer to a fractional area of rocks ≥ 1 m in diameter, which is supposed to be well represented by the Diviner data.

The statistical values derived from our rock detection results are shown in the second row in Table 6. Note that for some datasets no statistical value can be obtained, as the minimum rock size that can be recognized from the images is larger than 1 m in diameter. Based on the k values and our rock abundance model, for each study area, the fractional area of rocks $\geq 1\text{m}$ in diameter can be estimated, which is then compared with the average value of the Diviner bins covering the same area. According to Table 6, the largest difference is between the model value and the Diviner value in the Zi Wei (C1) crater area and is less than 0.02, which indicates that both our statistical results and the model values are in good agreement with the Diviner data.

4.3.2 Comparison in the Oceanus Procellarum area

To have a more comprehensive comparison with the Diviner data, a rock abundance map (Figure 17 (a)) is generated based on the proposed rock abundance model and the actual rocks detected from the LRO NAC image mosaic (1.5 m/pixel) in the Oceanus Procellarum study area, by binning the detected rocks into pixels covering the same region of each Diviner bin. The same geographic coordinate system (GCS_MOON_2000) and the same map projection (Mercator) were used for the Diviner data and the LRO NAC image mosaic to make the comparison. Similar to the four local selected regions 1- 4 in this area as discussed previously, the rock abundance k value corresponding to each pixel is determined based on the fractional area of rocks $\geq 3\text{ m}$ in diameter (the minimum size that can be recognized from the image) to reduce the uncertainties caused by low image resolution. From the k value and the proposed rock abundance model, the fractional area covered by rocks $\geq 1\text{ m}$ in diameter can be determined for each pixel in the map, which can then be compared with the Diviner

map. As a reference, the detected rocks are shown in Figure 17 (d). According to the generated map, the highest rock fractional area in this area is 0.2515, and the average fractional value is 0.0037, while the highest and average values derived from the Diviner data (see Figure 17(b)) are 0.2451 and 0.0051, respectively. Note that the average fractions shown in Figure 17(a) and (b) are close to the global average rock areal fraction of 0.004 [Bandfield *et al.*, 2011]. Despite the favorable consistency, differences exist between our results and the Diviner data. By comparing Figure 17(a) and (b), we find that our map shows clear feature (mainly crater) shapes, while the features (particularly small craters and the thin lava flow) are prone to a vague representation on the Diviner rock abundance map, which again indicates that the Diviner data are likely to fail to accurately describe the rock abundance information around small ground features. The reason for this could be that the rock abundance algorithm in Bandfield *et al.* [2011] is sensitive to the differences in temperatures within a measurement field of view (FOV). Therefore, if the FOV contains small terrain features with various slopes inside and outside, the measurement would include a range of temperatures, which would result in the algorithm likely being erroneous at some level. There are also potentially real rock-related explanations for the differences, especially since the rock size sensitivity of the Diviner data can be complicated. In addition, a cluster of smaller rocks may mimic the thermal properties of larger rocks. Apart from that, the size difference between rocks derived from LRO NAC images (rocks \geq 3 m in diameter) and from the Diviner data (rocks \geq ~1 m in diameter) might also lead to differences in the results if the size frequency distribution does not apply well at very low rock fractions.

A detailed comparison is shown in Figure 17(c), which is generated by the rock areal fraction estimated by our model minus that from the Diviner data. It shows that the largest positive

difference is 0.063, the largest negative difference is -0.124, and the average absolute difference is 0.003.

In general, as illustrated in Figure 18, the differences between our results and the Diviner data are distributed with a pattern that shows that our estimated rock areal fraction is higher than the fraction estimated using the Diviner data within a crater but lower outside the crater. In the region outside the crater (the black box in Figure 17(d)), our estimated rock areal fraction is quite close to 0, but the Diviner data show a high value. However, as indicated by the zoomed-in view of the area in Figure 16(e), this area is nearly rock-free. This can be explained by the heat conduction between the crater and the surrounding regolith surface. Further, according to Bandfield *et al.* [2011], the Diviner observations can be affected by latitude, local time, and local slope, which will consequently lead to deviations in the final rock abundance estimation.

There are also situations where our estimated rock areal fraction is lower than the fraction estimated using the Diviner data within a crater, as shown in Figure 19, which is caused by the failure of rock detection in shadow areas. Generally, the shadows are caused by high solar incidence angle and the repose angle of the lunar regolith. Selecting images with low solar incidence angle could alleviate this problem.

5. Analyses on Rock Abundance and Surface Maturity in the Oceanus Procellarum Area

Based on the rock detection results and the derived rock abundance model, this paper further investigates the relationships between rock abundance and surface maturity by means of crater morphology and other crater characteristics, using the dataset in the Oceanus Procellarum area.

5.1 Rock Abundance and Crater Depth-to-Diameter Ratio

According to Figure 17, there is a clear correlation between craters and rock abundance values, as both craters and rocks may result from impacts. However, rocks are prone to degrade with increasing ages [Mendell, 1976; Thompson *et al.*, 1974], which mean younger craters are likely to present higher rock abundance. Basilevsky *et al.* [2013] analyzed the abundance of rocks (≥ 2 m in diameter) on the rims of twelve craters (150-950 m in diameter) with known ages to estimate the survival time of rocks, and found that when 50% and 90% of the rocks are destroyed, the survival time is estimated to be around 40-80 Ma and around 150-300 Ma, respectively. Ghent *et al.* [2014] also investigated the erosion rate of large ejected rocks on lunar surface based on rock abundance derived from Diviner data and found that there is a strong inverse correlation between the rock abundance value and the crater age. Similarly, the morphological features of impact craters also change over time [Head, 1975], and one embodiment is that old craters show a remarkable degree of shallowing compared with younger craters with similar diameter [Pike, 1969; 1971]. To further investigate the correlation between rock abundance and crater morphology, we measured the depth-to-diameter ratio of 121 craters using ArcGIS in the study area in Oceanus Procellarum (as shown in Figure 20). The diameters of these craters were manually measured from the 1.5 m/pixel LRO NAC image mosaic (Figure 20 (a)) along the illumination direction, and the

depths were determined by the average elevation of surrounding regolith minus the minimum elevation of crater floors measured in profiles generated from a 60 m/pixel DEM (Figure 20 (b)), which is the SLDEM generated by co-registering the DEM from Selenological and Engineering Explorer (SELENE) Terrain Camera images and the Lunar Orbiter Laser Altimeter (LOLA) data. The SLDEM has a vertical uncertainty of ~2.44 m [Barker *et al.*, 2016]. The LRO NAC image mosaic and the SLDEM were originally co-registered.

To evaluate the uncertainties in determining the depth-to-diameter ratio of craters, we repeatedly measured the diameters and depths of four craters with representative sizes (diameters of ~3000 m, ~2000 m, ~1000 m, and ~300 m, respectively) on 20 different diameter directions along the crater rim, and computed the uncertainty of the depth-to-diameter ratio based on the error propagation. The results indicate that the uncertainty of depth-to-diameter ratio increases with the crater size getting smaller. The maximum uncertainty of the depth-to-diameter ratio is ± 0.0124 , corresponding to the smallest crater of the total 121 selected craters.

The maximum rock abundance corresponding to each crater was measured from the rock abundance map shown in Figure 17 (a), which was generated based on the rock detection results and rock abundance model. Figure 21 shows the maximum rock abundance values versus the depth-to-diameter ratio of craters. In general, the maximum rock abundance value increases with the growing of the depth-to-diameter ratio. However, this increasing trend fluctuates within a certain range, which may be caused by the complexities of the formation and evolution of lunar craters [Head, 1975; Pike, 1969; 1971]. In Figure 21, all the plots are located between two parallel lines

$$\begin{cases} F = 2.6032r - 0.0964 \\ F = 2.6047r - 0.2988 \end{cases} \quad (9)$$

where F is the maximum rock abundance value corresponding to the crater area and r is the depth-to-diameter ratio of the crater. These two lines suggest that the fluctuation range of the maximum rock abundance corresponding to a crater area with a certain depth-to-diameter ratio is around 20%.

The above Equation (9) provides a useful mean to estimate the rock abundance around a crater area based on the crater depth-to-diameter ratio, which is useful for related scientific studies. The correlation between rock abundance and crater depth-to-diameter ratio also provides clues to infer the crater maturity and surface maturity from rock abundance maps either generated from our approach or by Diviner data.

5.2 Rock Abundance and Crater Ray Brightness

From the above 121 craters, it is also found that craters with higher rock abundance show brighter crater rays than those with lower rock abundance values, and this is especially true for craters smaller than 1 km in diameter (see Figure 22(a) – (h)). According to *Hawke et al.* [2004], lunar ray brightness degrades with increasing age and surface maturity, therefore it can also be assumed that craters with higher rock abundance are likely to be younger craters.

The crater shown in Figure 22 (i) (in fact it is also the selected region #1 shown in Figure 8 (e), Figure 9 (a) and Figure 16 (e)) has the highest depth-to-diameter ratio of 0.147 and also

the highest rock abundance value of 25.1% among all the measured craters in the study area. It shows brighter crater rays in comparison with the crater in Figure 22 (j), which has similar diameter but lower depth-to-diameter ratio and lower rock abundance value.

Figure 22 (k) and (l) show two craters larger than 2 km in diameter with the maximum and minimum rock abundance values of 22.4% and 3.9%, respectively. These two craters have similar diameter and depth-to-diameter ratio. The one with higher rock abundance shows higher albedo properties, which indicates that this crater is fresher than the other one [Hawke *et al.*, 2004]. Overall, the rock abundance seems to be correlated with the surface maturity, and craters with high rock abundance are likely to have relatively younger age as suggested by the presence of bright crater rays and high albedo.

6. Conclusions and Discussion

High-resolution lander descent images and LRO NAC images can assist in acquiring information about the rock distribution and rock abundance on the lunar surface on a large scale. Therefore, a novel rock detection approach is proposed to automatically identify rocks from such high-resolution imagery. Based on the rock detection results from high-resolution images, a rock abundance model is derived by fitting the rock size-frequency distributions into exponential curves. The rock abundance model makes it feasible to estimate the overall cumulative fractional area covered by rocks with different sizes on lunar surface. Note that the minimum size of rocks that can be recognized from images is always limited by the image resolution, therefore the proposed rock abundance model extends the current research on rock

distributions on lunar surface, which is of significance for lunar regolith research and landing site selection for future missions.

Our rock detection results and rock abundance model are compared with those of previous studies by Di *et al.* [2016] and Bandfield *et al.* [2011]. The comparison with Di *et al.* [2016] at the Chang'E-3 landing site indicates that, although the rock size–frequency distributions at very small waypoint sites show more randomness than agreement with our rock abundance model, the overall result agrees well with our model. A comprehensive comparison with the rock abundance map derived from the Diviner data [Bandfield *et al.*, 2011] is also made and analyzed. In general, our results are consistent with the Diviner results in both the selected local regions and the large area in Oceanus Procellarum, which indicates the reliability and effectiveness of our rock detection approach and the rock abundance model. A more detailed comparison suggests that our results perform better than the Diviner results in describing rock abundance around small ground features.

By analyzing the rock abundance and the crater morphology and other characteristics in the Oceanus Procellarum area, it is found that craters with high depth-to-diameter ratio or bright crater rays (or high albedo) are likely to have high rock abundance values. The investigation indicates that the rock abundance has a certain correlation with the regolith age, which is consistent with the findings in Mendell [1976] and Thompson *et al.* [1974], and craters with higher rock abundance are likely to be relatively younger.

This research also has certain limitations. First, the proposed approach detects rocks mainly on the basis of the gradient differences in the illumination direction, which implies that to some extent, the performance of the approach is limited by the illumination conditions during image acquisition. Second, when the incidence angle of the sunlight is very small, shadows are observed on the incidence sides of deep craters, and these shadows in the images will directly lead to a failure of the rock detection in the shadow areas. Therefore, in future work, we intend to combine high-resolution imagery and other types of data sources, such as radar and TIR observations, for more accurate rock detection, with which our rock abundance model will be further tested in relatively vast regions.

Acknowledgments

The work described in this paper was funded by a grant from the Research Grants Council of Hong Kong (Project No: PolyU 152086/15E) and a grant from the National Natural Science Foundation of China (Project No: 41671426). The detected rock distribution data are archived in Zenodo (https://zenodo.org/record/1203295/files/moon_rock_distribution_data.rar). The LRO NAC images used in this research are available at the LRO Archive (<http://lroc.sese.asu.edu/>) by referring to the image ID described in the paper. The authors would like to thank all those who worked on the archive of the datasets to make them publicly available.

References

- Adams, R., and L. Bischof (1994), Seeded region growing, *IEEE Transactions on pattern analysis and machine intelligence*, 16(6), 641-647.
- Aldrin Jr, E. E., N. A. Armstrong, and M. Collins (1969), Crew observations, NASA Special Publication, 214, 35.
- Arvidson, R., D. Adams, G. Bonfiglio, P. Christensen, S. Cull, M. Golombek, J. Guinn, E. Guinness, T. Heet, and R. Kirk (2008), Mars Exploration Program 2007 Phoenix landing site selection and characteristics, *Journal of Geophysical Research: Planets*, 113(E3).
- Bandfield, J. L., R. R. Ghent, A. R. Vasavada, D. A. Paige, S. J. Lawrence, and M. S. Robinson (2011), Lunar surface rock abundance and regolith fines temperatures derived from LRO Diviner Radiometer data, *Journal of Geophysical Research: Planets*, 116(E12).
- Barker, M., E. Mazarico, G. Neumann, M. Zuber, J. Haruyama, and D. Smith (2016), A new lunar digital elevation model from the Lunar Orbiter Laser Altimeter and SELENE Terrain Camera, *Icarus*, 273, 346-355.
- Bart, G., and H. Melosh (2010), Impact into lunar regolith inhibits high-velocity ejection of large blocks, *Journal of Geophysical Research: Planets*, 115(E8).
- Basilevsky, A., A. Abdrakhimov, J. Head, C. Pieters, Y. Wu, and L. Xiao (2015), Geologic characteristics of the Luna 17/Lunokhod 1 and Chang'E-3/Yutu landing sites, northwest Mare Imbrium of the Moon, *Planetary and Space Science*, 117, 385-400.
- Basilevsky, A., J. Head, and F. Horz (2013), Survival times of meter-sized boulders on the surface of the Moon, *Planetary and Space Science*, 89, 118-126.
- Canny, J. (1986), A computational approach to edge detection, *IEEE Transactions on pattern analysis and machine intelligence*(6), 679-698.
- Christensen, P. R. (1986), The spatial distribution of rocks on Mars, *Icarus*, 68(2), 217-238.

-
- Cintala, M. J., and K. M. McBride (1995), Block distributions on the lunar surface: A comparison between measurements obtained from surface and orbital photography.
- Crawford, I. A., and K. H. Joy (2014), Lunar exploration: opening a window into the history and evolution of the inner Solar System, *Philosophical Transactions of the Royal Society of London A: Mathematical, Physical and Engineering Sciences*, 372(2024), 20130315.
- Crawford, I. A., K. H. Joy, and M. Anand (2014), Lunar exploration, *The Encyclopedia of the Solar System*, 3rd edition. Amsterdam: Elsevier, 555579.
- De Rosa, D., B. Bussey, J. T. Cahill, T. Lutz, I. A. Crawford, T. Hackwill, S. van Gasselt, G. Neukum, L. Witte, and A. McGovern (2012), Characterisation of potential landing sites for the European Space Agency's Lunar Lander project, *Planetary and Space Science*, 74(1), 224-246.
- Di, K., B. Xu, M. Peng, Z. Yue, Z. Liu, W. Wan, L. Li, and J. Zhou (2016), Rock size-frequency distribution analysis at the Chang'E-3 landing site, *Planetary and Space Science*, 120, 103-112.
- Gao, W., X. Zhang, L. Yang, and H. Liu (2010), An improved Sobel edge detection, paper presented at Computer Science and Information Technology (ICCSIT), 2010 3rd IEEE International Conference on, IEEE.
- Ghent, R. R., P. O. Hayne, J. L. Bandfield, B. A. Campbell, C. C. Allen, L. M. Carter, and D. A. Paige (2014), Constraints on the recent rate of lunar ejecta breakdown and implications for crater ages, *Geology*, 42(12), 1059-1062.
- Gilvarry, J. (1961), Fracture of brittle solids. I. Distribution function for fragment size in single fracture (theoretical), *Journal of Applied Physics*, 32(3), 391-399.
- Gilvarry, J., and B. Bergstrom (1961), Fracture of brittle solids. II. Distribution function for fragment size in single fracture (experimental), *Journal of applied physics*, 32(3), 400-410.

-
- Golombek, M., R. Arvidson, J. Bell III, and P. Christensen (2005), Assessment of Mars Exploration Rover landing site predictions, *Nature*, 436(7047), 44.
- Golombek, M., R. Cook, H. Moore, and T. Parker (1997), Selection of the Mars Pathfinder landing site, *Journal of Geophysical Research: Planets*, 102(E2), 3967-3988.
- Golombek, M., J. Grant, D. Kipp, A. Vasavada, R. Kirk, R. Fergason, P. Bellutta, F. Calef, K. Larsen, and Y. Katayama (2012a), Selection of the Mars Science Laboratory landing site, *Space science reviews*, 170(1-4), 641-737.
- Golombek, M., J. Grant, T. Parker, D. Kass, J. Crisp, S. Squyres, A. Haldemann, M. Adler, W. Lee, and N. Bridges (2003a), Selection of the Mars Exploration Rover landing sites, *Journal of Geophysical Research: Planets*, 108(E12).
- Golombek, M., A. Huertas, D. Kipp, and F. Calef (2012b), Detection and characterization of rocks and rock size-frequency distributions at the final four Mars Science Laboratory landing sites, *International Journal of Mars Science and Exploration*, 7, 1-22.
- Golombek, M., A. Huertas, J. Marlow, B. McGrane, C. Klein, M. Martinez, R. Arvidson, T. Heet, L. Barry, and K. Seelos (2008), Size-frequency distributions of rocks on the northern plains of Mars with special reference to Phoenix landing surfaces, *Journal of Geophysical Research: Planets*, 113(E3).
- Golombek, M., D. Kipp, N. Warner, I. J. Daubar, R. Fergason, R. L. Kirk, R. Beyer, A. Huertas, S. Piqueux, and N. Putzig (2017), Selection of the InSight landing site, *Space Science Reviews*, 1-91.
- Golombek, M., and D. Rapp (1997), Size-frequency distributions of rocks on Mars and Earth analog sites: Implications for future landed missions, *Journal of Geophysical Research: Planets*, 102(E2), 4117-4129.
- Golombek, M. P., L. Crumpler, J. A. Grant, R. Greeley, N. Cabrol, T. Parker, J. W. Rice, J. Ward, R. E. Arvidson, and J. Moersch (2006), Geology of the Gusev cratered plains from

the Spirit rover transverse, *Journal of Geophysical Research: Planets*, 111(E2).

Golombek, M. P., A. Haldemann, N. Forsberg□Taylor, E. DiMaggio, M. Mellon, and J. Matijevic (2003b), Rock size□frequency distributions on Mars and implications for Mars Exploration Rover landing safety and operations, *Journal of Geophysical Research: Planets*, 108(E12).

Grott, M., J. Knollenberg, and C. Krause (2010), Apollo lunar heat flow experiment revisited: a critical reassessment of the in situ thermal conductivity determination, *Journal of Geophysical Research: Planets*, 115(E11).

Hawke, B. R., D. Blewett, P. Lucey, G. Smith, J. Bell, B. Campbell, and M. Robinson (2004), The origin of lunar crater rays, *Icarus*, 170(1), 1-16.

Head, J. W. (1975), Processes of lunar crater degradation-Changes in style with geologic time, *Moon*, 12, 299-329.

Heet, T. L., R. Arvidson, S. Cull, M. Mellon, and K. Seelos (2009), Geomorphic and geologic settings of the Phoenix Lander mission landing site, *Journal of Geophysical Research: Planets*, 114(E1).

Huertas, A., Y. Cheng, and R. Madison (2006), Passive imaging based multi-cue hazard detection for spacecraft safe landing, paper presented at Aerospace Conference, 2006 IEEE, IEEE.

Keihm, S., and M. Langseth Jr (1973), Surface brightness temperatures at the Apollo 17 heat flow site: Thermal conductivity of the upper 15 cm of regolith, paper presented at Lunar and Planetary Science Conference Proceedings.

Langseth, M. G., S. J. Keihm, and K. Peters (1976), Revised lunar heat-flow values, paper presented at Lunar and Planetary Science Conference Proceedings.

Liu, Z., K. Di, M. Peng, W. Wan, B. Liu, L. Li, T. Yu, B. Wang, J. Zhou, and H. Chen (2015), High precision landing site mapping and rover localization for Chang'e-3 mission,

Science China Physics, Mechanics & Astronomy, 58(1), 1-11.

Mellon, M. T., B. M. Jakosky, H. H. Kieffer, and P. R. Christensen (2000), High-resolution thermal inertia mapping from the Mars global surveyor thermal emission spectrometer, *Icarus*, 148(2), 437-455.

Mendell, W. (1976), Degradation of large, period II lunar craters, paper presented at Lunar and Planetary Science Conference Proceedings.

Mendell, W., and F. Low (1974), Preliminary results of the Apollo 17 infrared scanning radiometer, *Earth, Moon, and Planets*, 9(1), 97-103.

Moore, H., and J. Keller (1991), Surface-material maps of Viking landing sites on Mars, A Bibliography of Planetary Geology and Geophysics Principal Investigators and their Associates, 1990-1991.

Moore, H. J., R. Hutton, G. Clow, and C. Spitzer (1987), Physical properties of the surface materials at the Viking landing sites on MarsRep. 2330-7102.

Muehlberger, W., R. Batson, E. Boudette, C. Duke, R. Eggleton, D. Elston, A. England, V. Freeman, M. Hait, and T. Hall (1972), Preliminary geologic investigation of the Apollo 16 landing site.

Nowicki, S., and P. Christensen (2007), Rock abundance on Mars from the thermal emission spectrometer, *Journal of Geophysical Research: Planets*, 112(E5).

Pajola, M., S. Rossato, E. Baratti, C. Mangili, F. Mancarella, K. McBride, and M. Coradini (2014), Simud Vallis floor: A joint landing site for both the ExoMars 2018 and the Mars 2020 rovers, paper presented at Eighth International Conference on Mars.

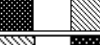
Pike, R. J. (1969), Meteoritic origin and consequent endogenic modification of large lunar craters-a study in analytic geomorphologyRep. 2331-1258, US Geological Survey.

Pike, R. J. (1971), Genetic implications of the shapes of martian and lunar craters, *Icarus*, 15(3), 384-395.

-
- Roelof, E. C. (1968), Thermal behavior of rocks on the lunar surface, *Icarus*, 8(1-3), 138-159.
- Sharifi, M., M. Fathy, and M. T. Mahmoudi (2002), A classified and comparative study of edge detection algorithms, paper presented at Information Technology: Coding and Computing, 2002. Proceedings. International Conference on, IEEE.
- Shoemaker, E., and E. Morris (1968), Size-frequency distribution of fragmental debris, Surveyor project final report, Part, 2, 86-102.
- Shorthill, R. W. (1970), Infrared moon: A review, *J. Spacecraft Rockets*, 7, 385-397.
- Smith, B. G. (1967), Boulder distribution analysis of the Luna 9 photographs, *Journal of Geophysical Research*, 72(4), 1398-1399.
- Thompson, D. R., and R. Castano (2007), Performance comparison of rock detection algorithms for autonomous planetary geology, paper presented at Aerospace Conference, 2007 IEEE, IEEE.
- Thompson, T., H. Masursky, R. Shorthill, G. Tyler, and S. Zisk (1974), A comparison of infrared, radar, and geologic mapping of lunar craters, *The Moon*, 10(1), 87-117.
- Thompson, T., J. Pollack, M. Campbell, and B. O'Leary (1970), Radar maps of the moon at 70 cm wavelength and their interpretation, *Radio Science*, 5(2), 253-262.
- Wu, B., F. Li, L. Ye, S. Qiao, J. Huang, X. Wu, and H. Zhang (2014). Topographic Modeling and Analysis of the Landing Site of Chang'E-3 on the Moon, *Earth and Planetary Science Letters*, 405(2014), 257-273.
- Zhao, J., L. Xiao, L. Qiao, T. D. Glotch, and Q. Huang (2017), The Mons Rümker Volcanic Complex of the Moon: A Candidate Landing Site for the Chang'E-5 Mission, *Journal of Geophysical Research: Planets*.
- Zheng, Y., Z. Ouyang, C. Li, J. Liu, and Y. Zou (2008), China's lunar exploration program: present and future, *Planetary and Space Science*, 56(7), 881-886.

Table 1. Typical brightness distributions of pixels with different gray levels (values of g_1 , g_2 ,

G_1 and G_2 are calculated for the pixels in the middle).

Pixel distribution → illumination direction	Possible case	g_1	g_2	G_1	G_2
	rock, shadow, ground	$-d$	$-2d$	$-3d$	d
	ground, shadow, small crater	$-2d$	$-d$	$-3d$	$-d$
	crater, ground, shadow of another crater	d	$-d$	0	$2d$
	shadow, ground, another rock	$-d$	d	0	$-2d$
	shadow, small crater, ground	d	$2d$	$3d$	$-d$
	ground, small rock, shadow	$2d$	d	$3d$	d
For large craters, the situation is likely to be					
	G_1	$-d$	0	$-2d$	$2d$
	G_2	d	0	$-2d$	$-2d$
For large rocks, the situation is likely to be					
	G_1	d	0	$2d$	$-2d$
	G_2	$-d$	0	$2d$	$2d$
(large rock contains only bright pixels)					
or					
	G_1	d	d	0	$-d$
	G_2	$-d$	d	$2d$	d
(large rock contains gray pixels)					

Note: ,  and  refer to the image pixels with bright, medium, and dark gray levels, respectively.

Table 2. Key parameters from the labels and the estimated illumination directions of the LRO NAC images and the NAC mosaic

Image	Coverage	Spatial resolution (m/pixel)	Solar incidence angle	Solar azimuth	Estimated illumination direction
M1116664800	20.09 ~ 19.36°W, 43.96 ~ 45.26°N	1.10	44.83°W	17.66°	21°
M175502049	35.06 ~ 34.91°W, 37.75 ~ 38.71°N	0.35	57.78°E	310.05°	308°
M174868307	62.11 ~ 62.25°E, 12.16 ~ 13.13°N	0.30	40.40°E	289.40°	292°
LRO NAC mosaic	55 ~ 49 W, 41 ~ 45 N	1.50	--	--	--

Table 3. Rock detection results in the experimental areas.

	Spatial resolution (m/pixel)	Total number	Total area (m ²)	Areal fraction	Min. diameter (m)	Max. diameter (m)
C2 crater	0.05-0.1	122	13.58	0.058	0.13	2.52
Yutu traverse area	0.02-0.13	370	11.91	0.009	0.06	1.65
Chang'E-3 descent image covering area	0.02-0.17	1672	104.25	0.008	0.05	2.52
Zi Wei (C1) crater	1.1	449	3565.92	0.008	2.51	7.97
Tai Wei crater	1.1	635	4071.13	0.008	2.27	7.34
Luna 23	0.3	248	136.22	0.003	0.62	2.79
Luna 17	0.35	522	464.42	0.005	0.71	3.42
Oceanus Procellarum area	1.5	363,914	6,925,072	0.0002	3.0	40.31

Table 4. The correctness and completeness of the automated rock detection results in four local regions in Oceanus Procellarum.

Region	Total area of automatically detected rocks (A_1) (m^2)	Total area of manually digitized rocks (A_2) (m^2)	Total area of the true positive rocks (A_3) (m^2)	Correctness	Completeness
#1	186960.37	199614.44	156279.55	83.59%	78.29%
#2	9094.02	10725.96	8363.64	91.97%	77.97%
#3	74049.11	76383.86	64915.25	87.66%	84.98%
#4	4257.22	4914.38	3883.18	91.21%	79.01%
			Average	88.61%	80.06%

Table 5. Parameter values of the fitted curves for each dataset.

	C2 crater	Yutu traverse	Descent image covering area	Luna 17	Luna 23	Zi Wei (C1) crater	Tai Wei crater	#1	#2	#3	#4
k	0.0579	0.0119	0.0099	0.0159	0.0085	0.0612	0.0537	0.097	0.0117	0.0031	0.0025
q	0.699	1.781	1.798	1.469	1.995	0.753	0.75	0.289	0.902	0.344	0.873
R^2	0.9777	0.940	0.981	0.997	0.993	0.968	0.997	0.990	0.963	0.974	0.900

Table 6. Quantitative comparison with Diviner rock abundance map in different regions.

	Zi Wei (C1) crater	Tai Wei crater	Luna 17	Luna 23	#1	#2	#3	#4
Rock abundance k	6%	5.6%	1.5%	0.9%	20%	1.8%	2.6%	1.2%
Statistical value (Fractional area of rocks $\geq 1\text{m}$)	nil	nil	0.36%	0.10%	nil	nil	nil	nil
Model-fitted value (Fractional area of rocks $\geq 1\text{m}$)	2.75%	2.53%	0.36%	0.12%	10.66%	0.50%	0.90%	0.23%
Average Diviner value (Fractional area of rocks $\geq 1\text{m}$)	1.03%	0.93%	0.40%	0.60%	8.95%	0.64%	0.81%	0.36%
Difference	1.72%	1.60%	-0.04%	-0.48%	1.71%	-0.14%	0.09%	-0.13%

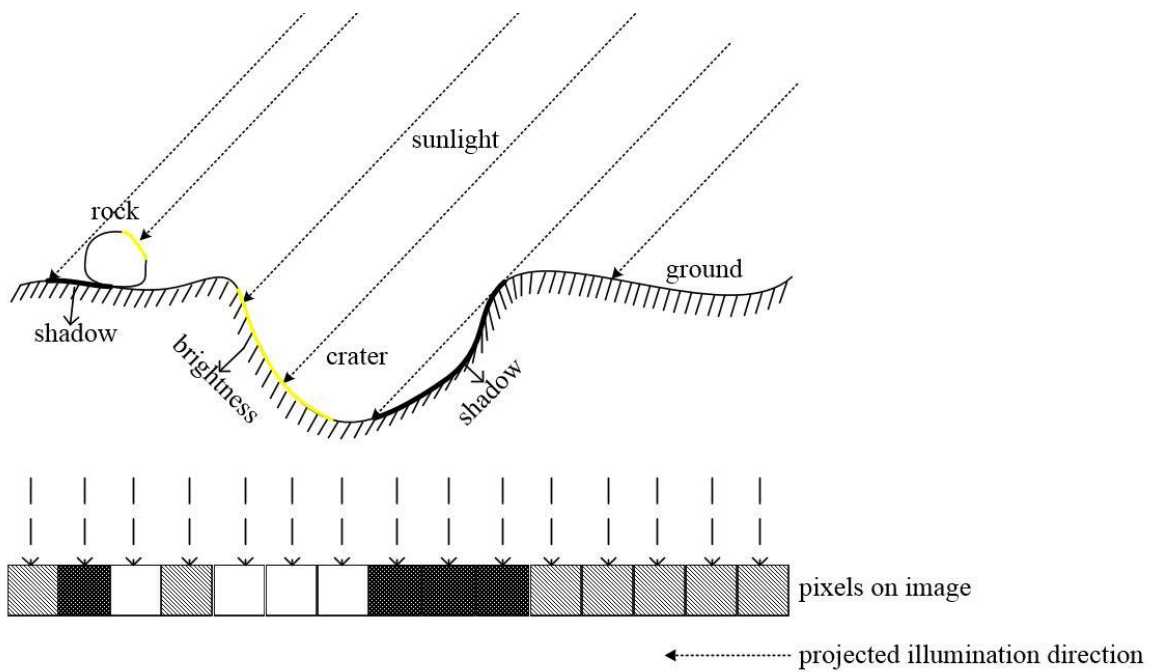


Figure 1. Imaging of terrain features and the brightness differences in the images.

Accepted

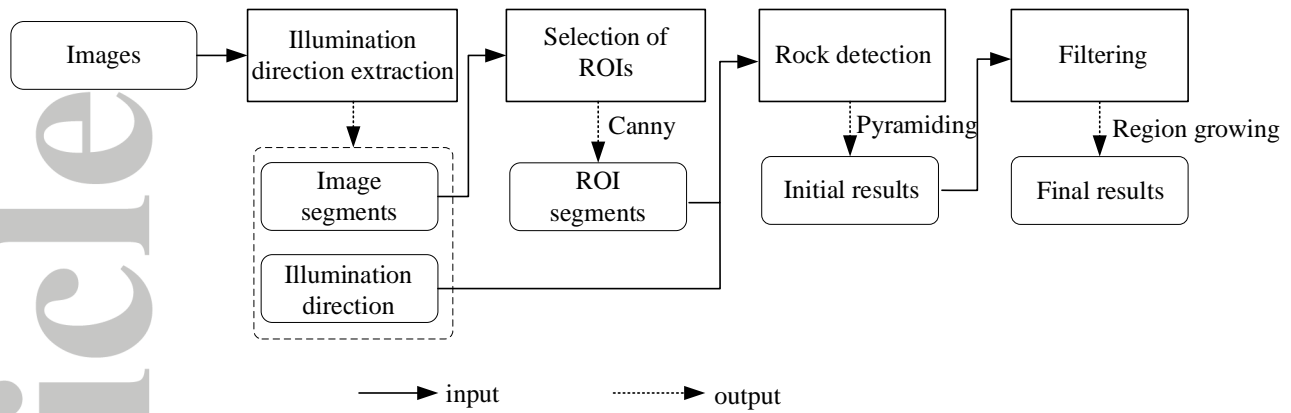


Figure 2. Overview of the rock detection approach.

Accepted Article

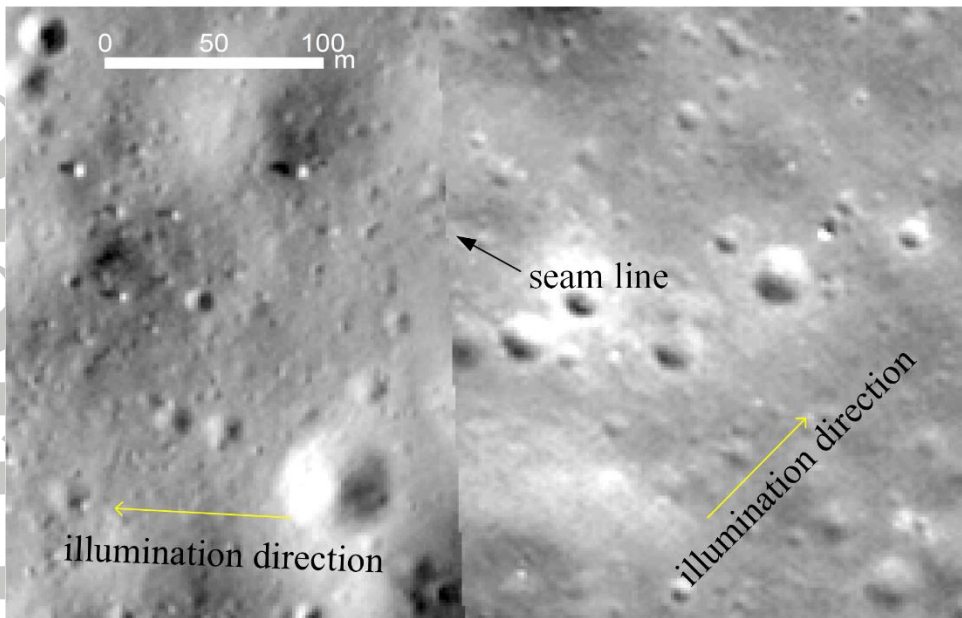


Figure 3. Example of the LRO NAC image mosaic showing different illumination directions.

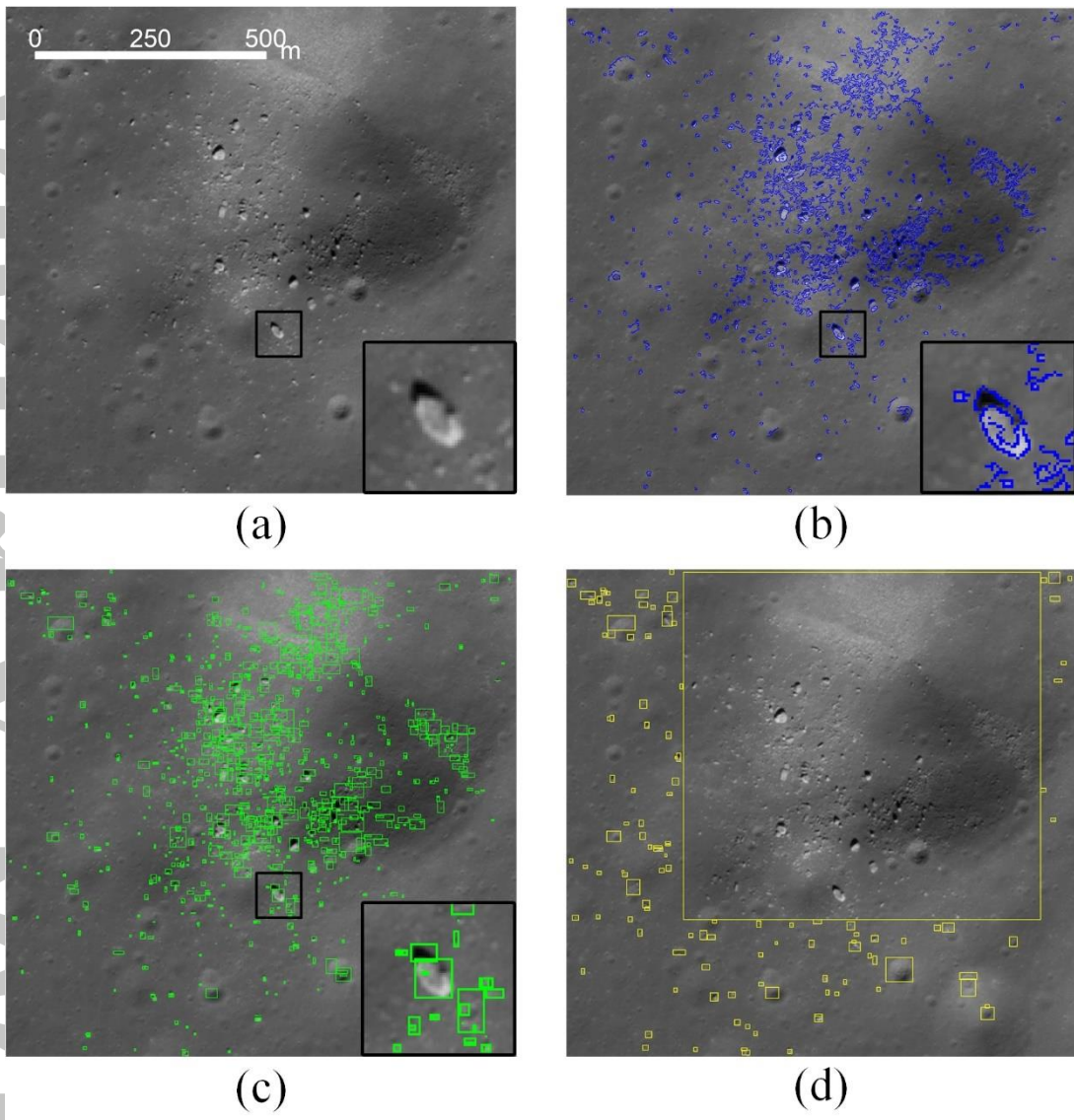


Figure 4. Selection of ROIs. (a) An original LRO NAC image, (b) edges (blue polygons) of rocks, craters, and shadows detected via Canny, (c) bounding rectangles (green) of detected edges, and (d) ROIs (yellow rectangles) generated by iteratively merging the overlapping bounding rectangles shown in (c). The black rectangles in (a), (b) and (c) show the location and enlarged views of a large rock in this area.

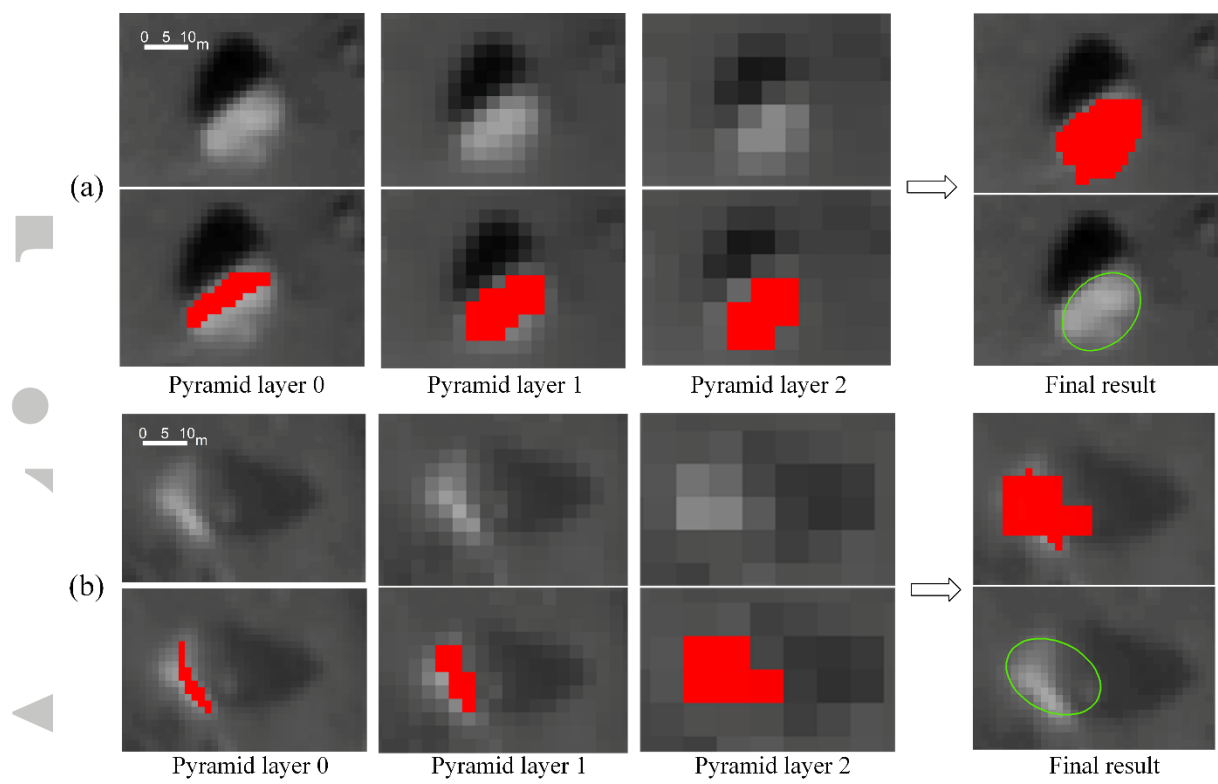


Figure 5. Detection of large rocks via image pyramiding. (a) A large rock contains only bright pixels, and (b) a large rock contains both bright and gray pixels caused by the convexity of the rock. The upper rows of (a) and (b) show the rocks presented on each pyramid layer, and the lower rows of (a) and (b) show the rock pixels highlighted with red for each pyramid layer. The last column shows the final results merged from all pyramid layers and the corresponding fitted ellipses.

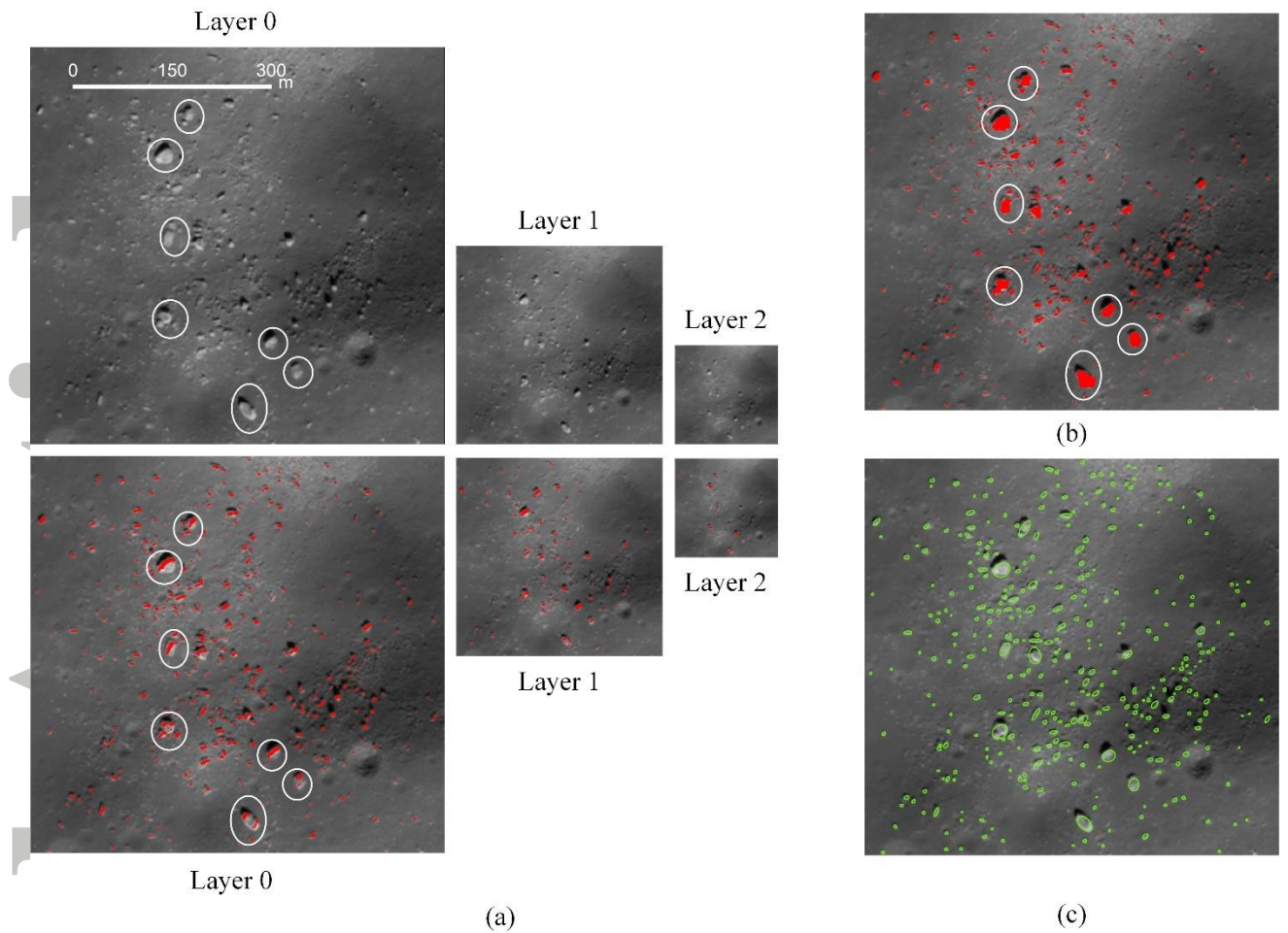


Figure 6. The overall procedure to detect rocks of varying sizes: (a) image pyramid of an ROI, where each higher layer is down-sampled from the lower layer while layer 0 is the original image. The rock pixels detected from each pyramid layer are marked with red, and some large rocks are marked with white circles; (b) the final merged rock detection result (the red pixels) on the original image, and (c) the fitted ellipses of rock boundaries (marked with green).

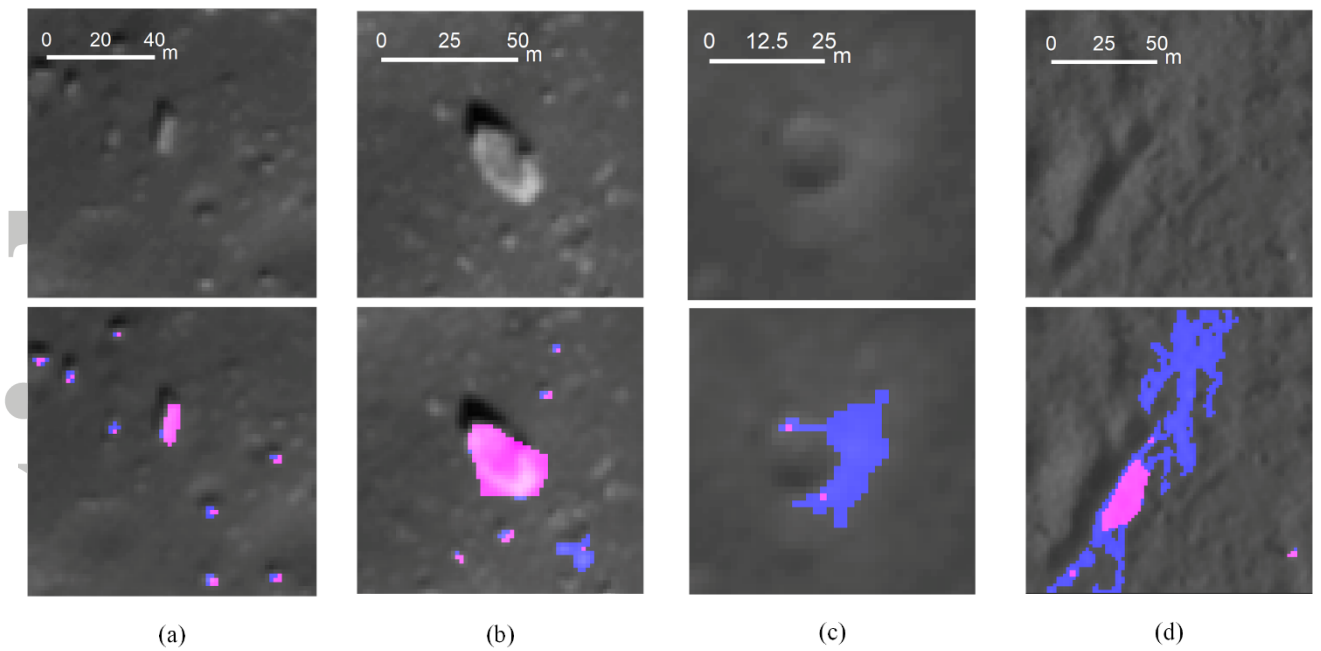


Figure 7. Region growing of the true and false detections for filtering false rocks. The upper row shows the original images, and the lower row shows the region growing results, where the rock pixels detected by our approach are highlighted with pink and the grown pixels, which are obtained through region growing, are highlighted with blue. (a) Region growing result of true detections of small rocks, (b) region growing result of true detections of large rocks, (c) region growing result of false detections around a crater, and (d) region growing result of false detections around a terrain relief.

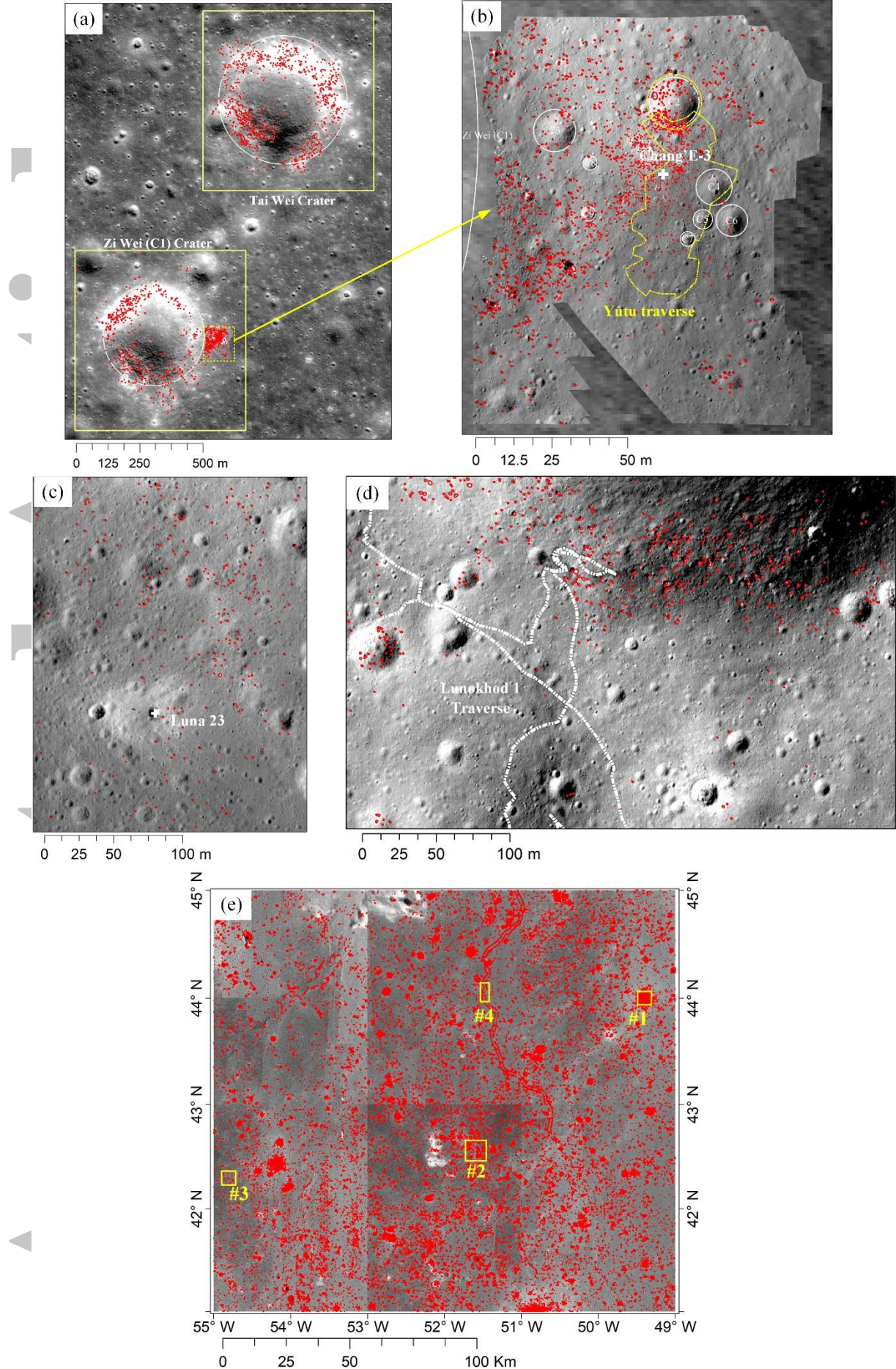


Figure 8. Orbital and descent images used for experiments with the detected rocks marked by red ellipses. (a) LRO NAC image M1116664800 (1.1 m/pixel) covering the Chang'E-3 landing area, (b) Chang'E-3 descent image mosaic, where the Chang'E-3 landing site is marked with a white cross; (c) LRO NAC image M174868307 (0.3 m/pixel) covering the Luna 23 landing site, where the Luna 23 landing site is marked with a white cross; (d) LRO NAC image M175502049 (0.35 m/pixel) covering the Luna 17 landing site, where the white dotted line referring to a partial traverse of Lunokhod 1; and (e) LRO NAC image mosaic (1.5 m/pixel) in the Oceanus Procellarum, and four local regions (#1 ~ #4) with typical landscapes are selected for quantitative evaluation.

Accepted Article

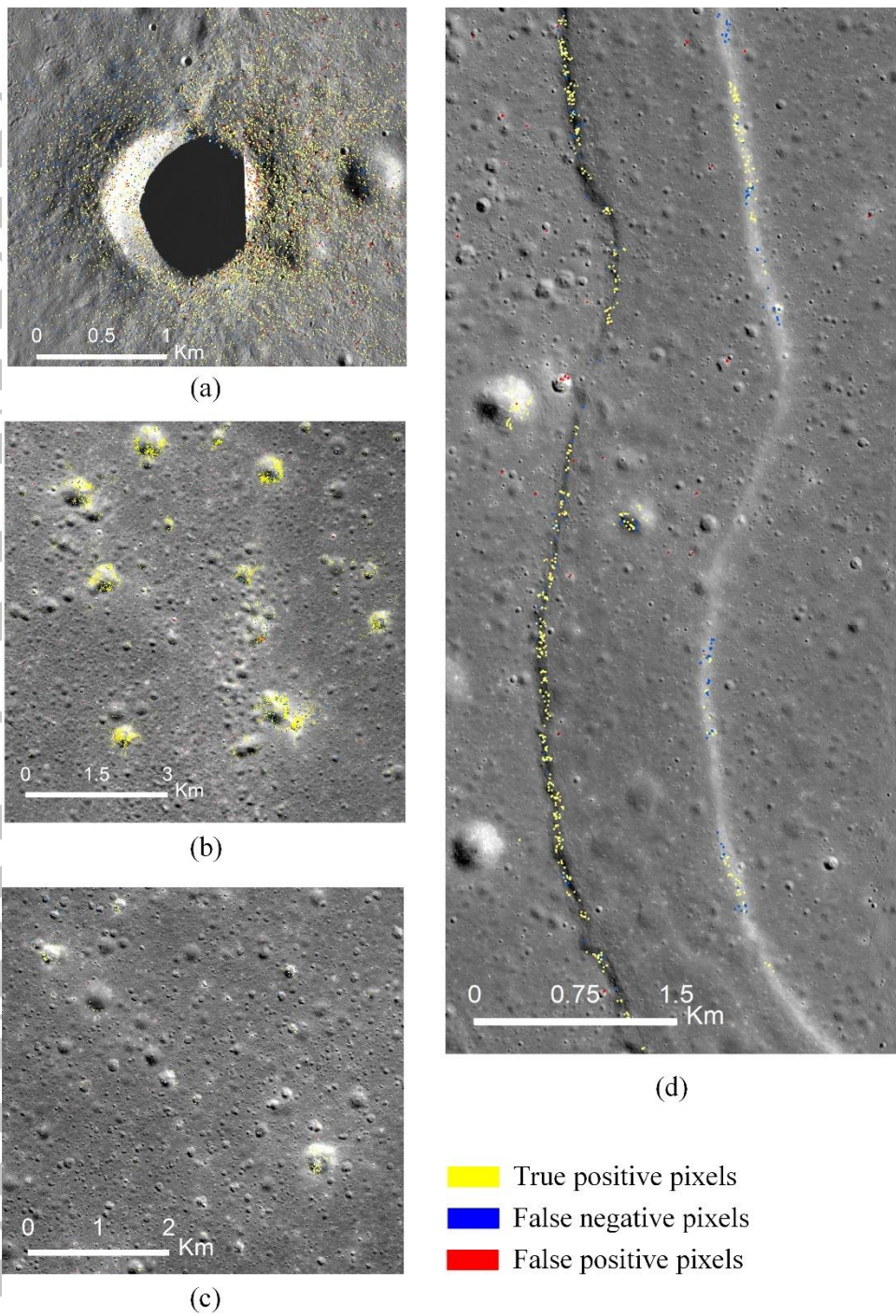


Figure 9. Benchmark results of four selected local regions (#1 ~ #4 in Figure 8(e)) in Oceanus Procellarum with typical geological characteristics. (a) Region 1 showing a typical large crater area with rocks distributed around the crater with a radiate pattern, (b) region 2 and (c) region 3 featured with many small craters, and (d) region 4 showing a part of the lava flow, along which most of the rocks are located at the slopes on two sides.

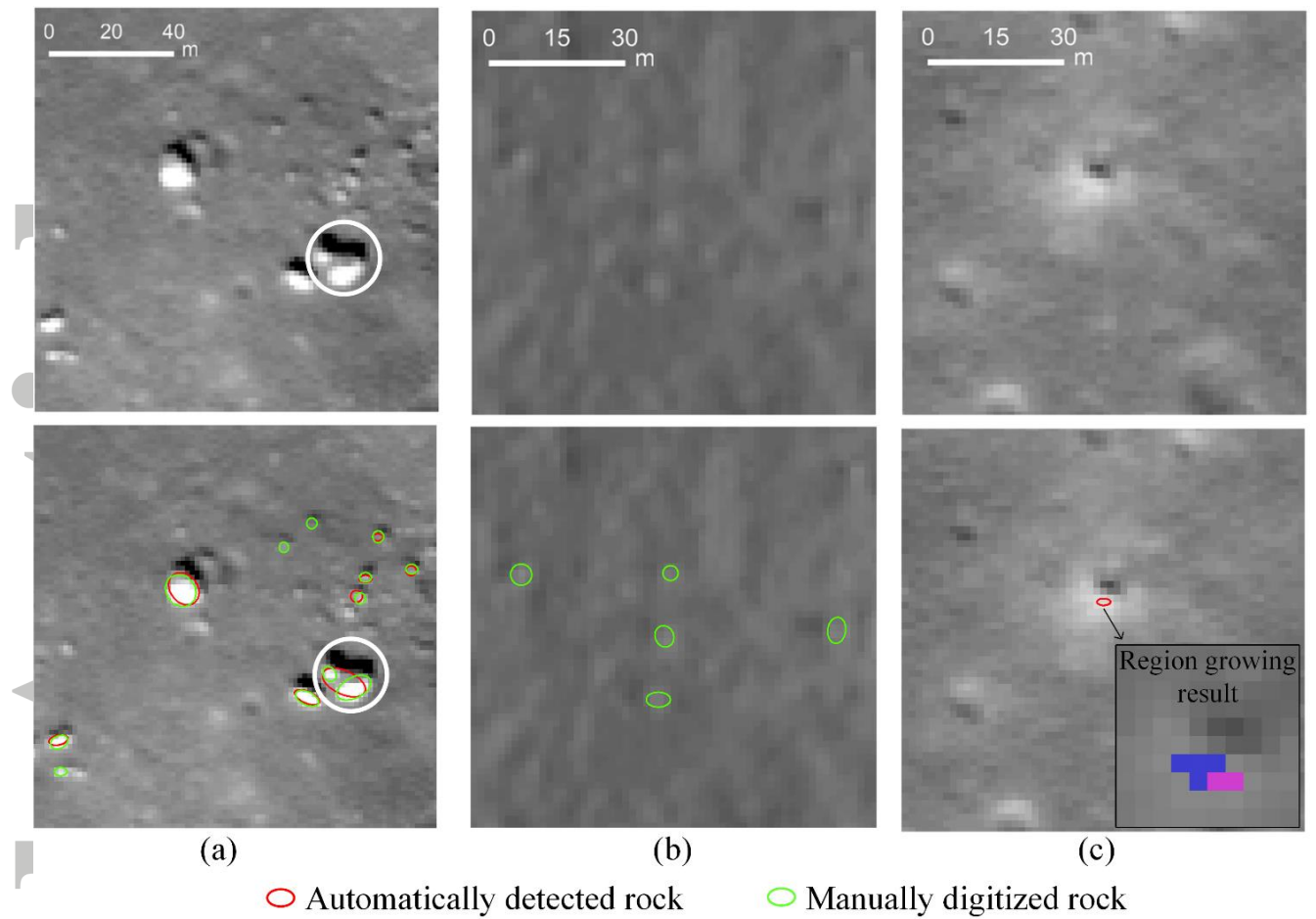


Figure 10. Comparison between the automatically detected rocks and manually digitized rocks (ground-truth). (a) True positive detections in a region where the brightness contrast between the rock pixels and the surrounding pixels is high, (b) false negative detections (omitted rocks) caused by the low contrast of brightness between the rocks and the surroundings, and (c) false positive detections around the boundary of a very small crater with high brightness contrast.

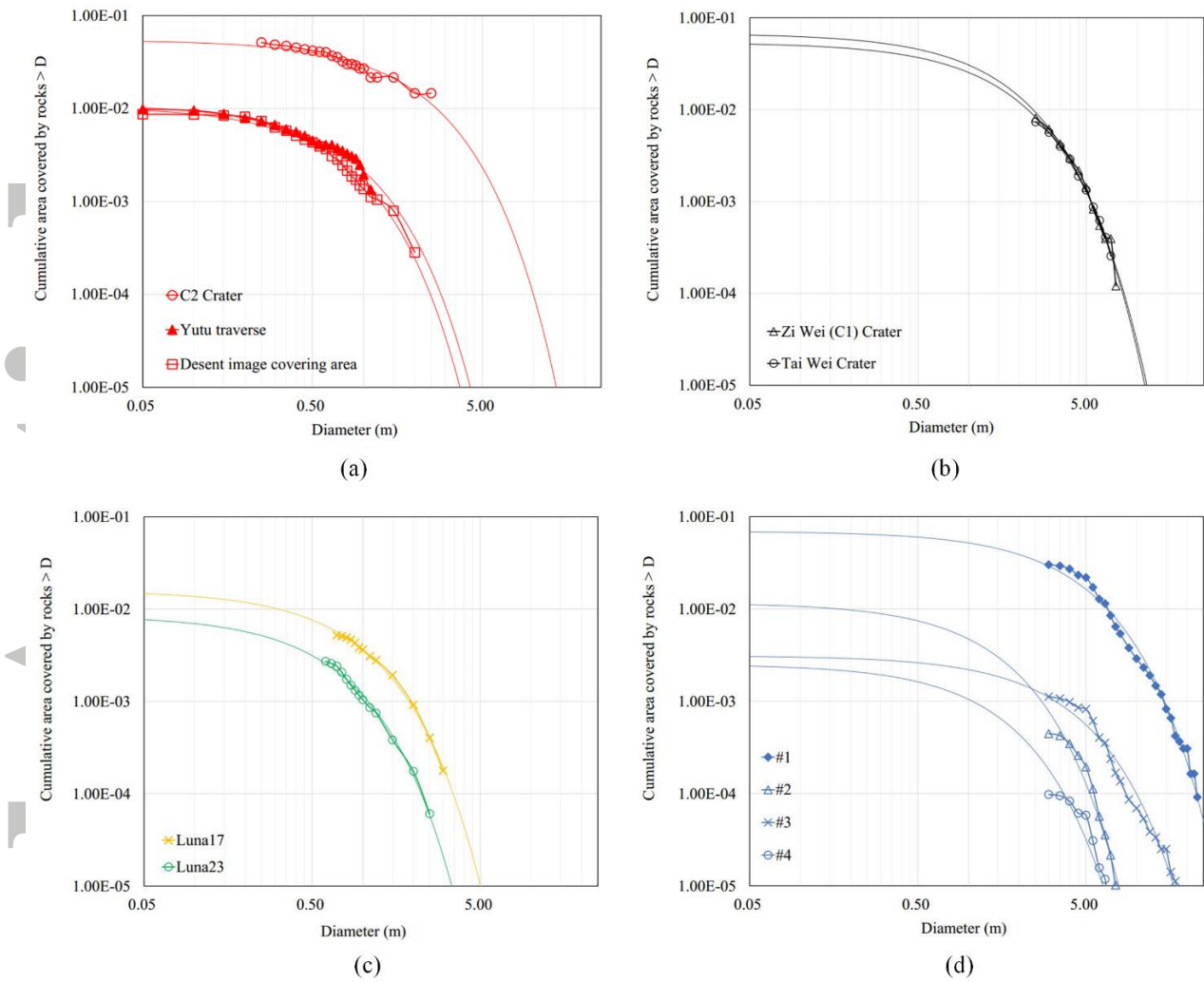


Figure 11. Cumulative fractional area of rocks versus diameter. (a) results derived from Chang'E-3 descent images, (b) results derived from LRO NAC image covering the Chang'E-3 landing area, (c) results derived from LRO NAC images covering the Luna 17 and 23 landing sites, and (d) results derived from LRO NAC image mosaic in the four selected regions in Oceanus Procellarum. The dotted curves show the size-frequency distributions of rocks detected from different images. Each of the dotted curves is fitted by a solid exponential curve with the same color.

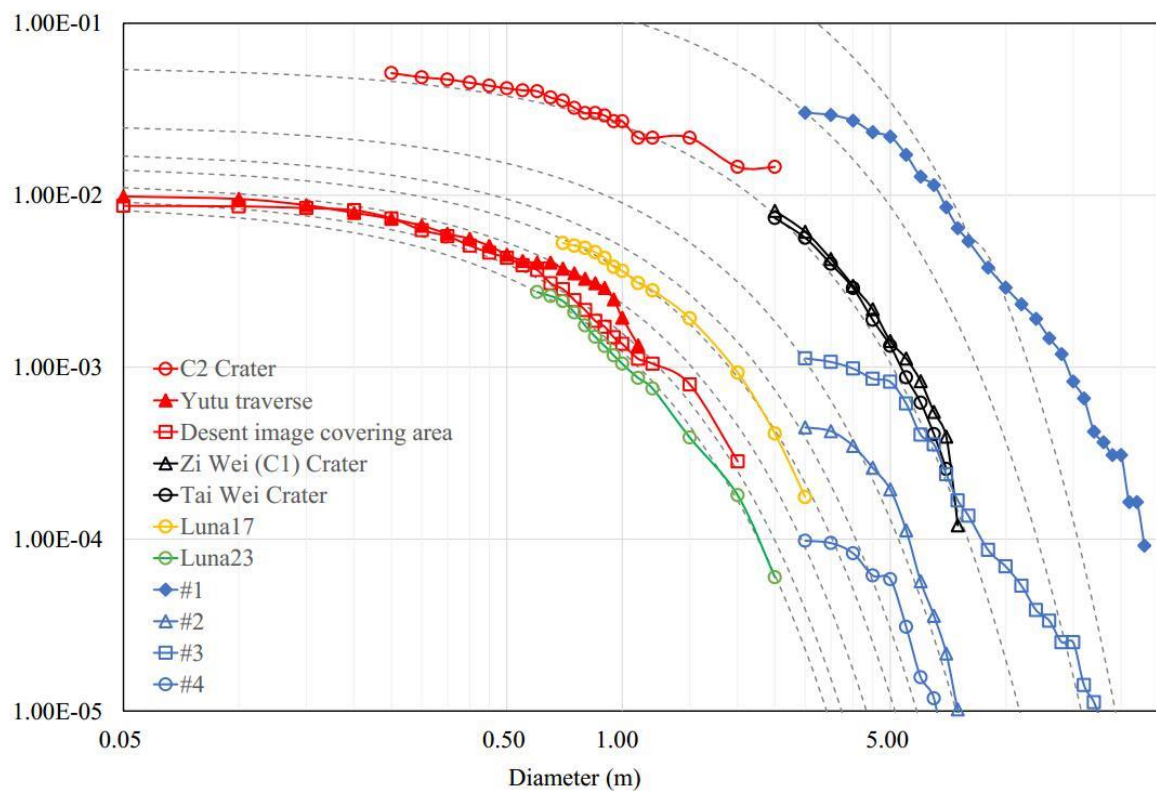


Figure 12. Comparison of the model and rock size-frequency curves. The colored curves are the size-frequency curves from the detected results, and the gray dashed curves are generated by the proposed rock abundance model. From left to right, the corresponding rock abundance k values are 0.9%, 1.0%, 1.2%, 1.5%, 2%, 3%, 6%, 24%, and 50%.

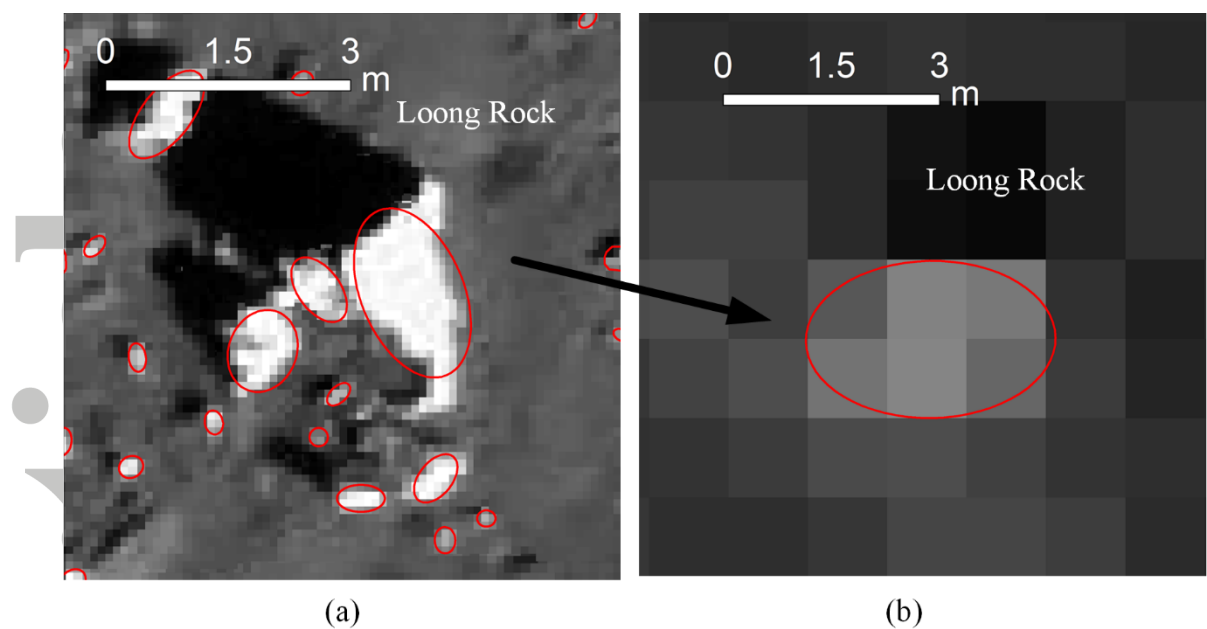


Figure 13. Rock detection results from images of the same area but with different resolutions. (a) A descent image with a resolution of 0.11 m/pixel, (b) an LRO NAC image with a resolution of 1.1 m/pixel. Both (a) and (b) show the Loong Rock [Di *et al.*, 2016] near the Chang'E-3 landing site.

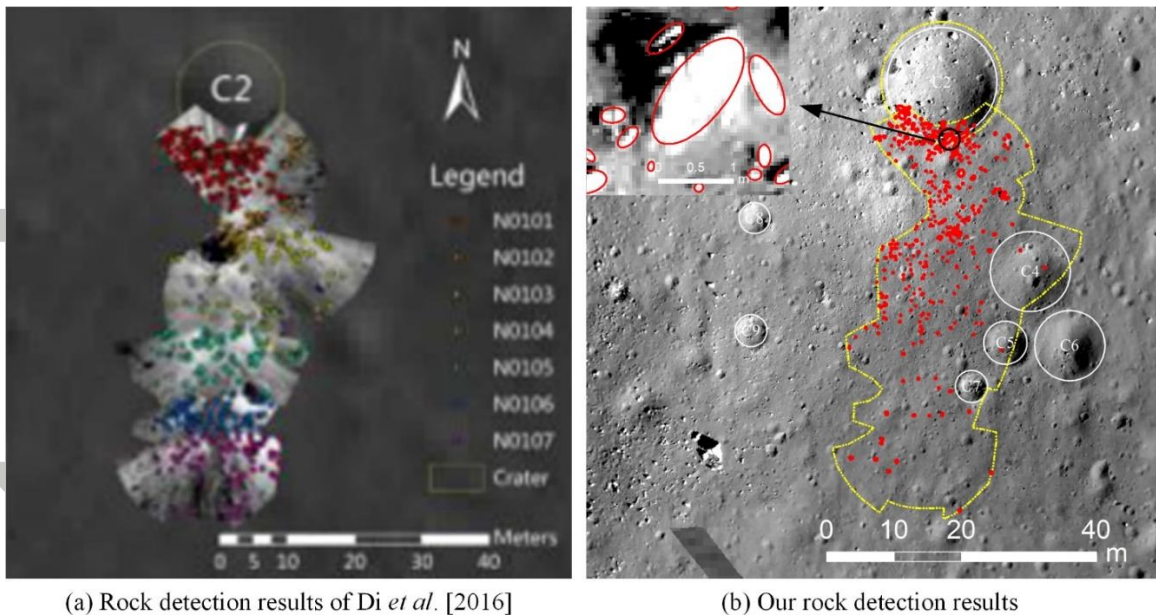


Figure 14. Comparison between the distributions of rocks detected in the same area. (a) rocks (highlighted by different colors at different waypoints) detected by Di *et al.* [2016] from the Yutu rover images, and (b) rocks (highlighted by red) detected by the proposed approach from the descent images, where the location of the largest rock with a diameter of 1.65 m is marked with a black circle.

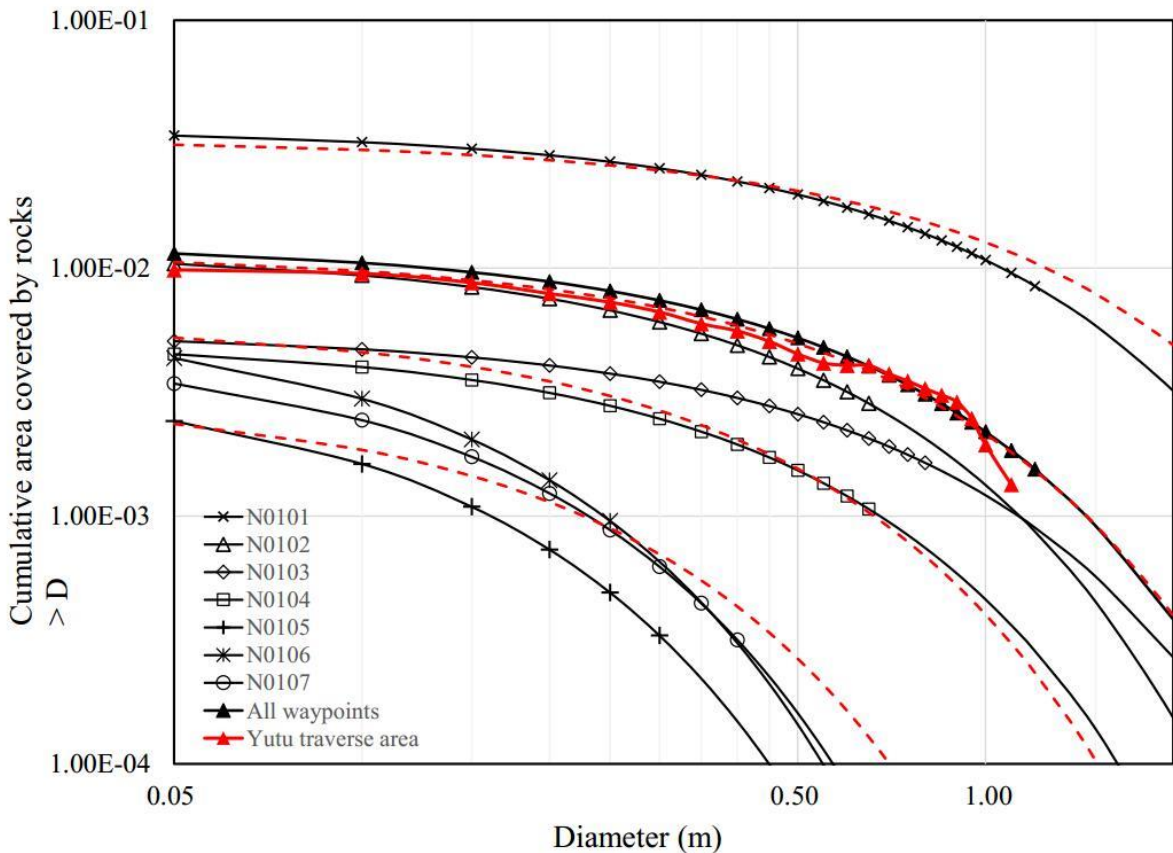


Figure 15. Comparison with the rock size–frequency distribution derived from the Chang'E-3 Yutu rover images [Di *et al.*, 2016], which covers the same area with the Yutu traverse area in this study. The red solid line with red triangles denotes the size–frequency distributions derived from the detected rocks in this area. The red dashed lines denote our model curves with a rock abundance of $k = 0.3\%$, $k = 0.6\%$, $k = 1.15\%$, and $k = 3.3\%$, respectively. The black lines refer to the fitted exponential curves obtained from the study by Di *et al.* [2016] for seven waypoints, as well as all waypoints, within the Yutu traverse area.

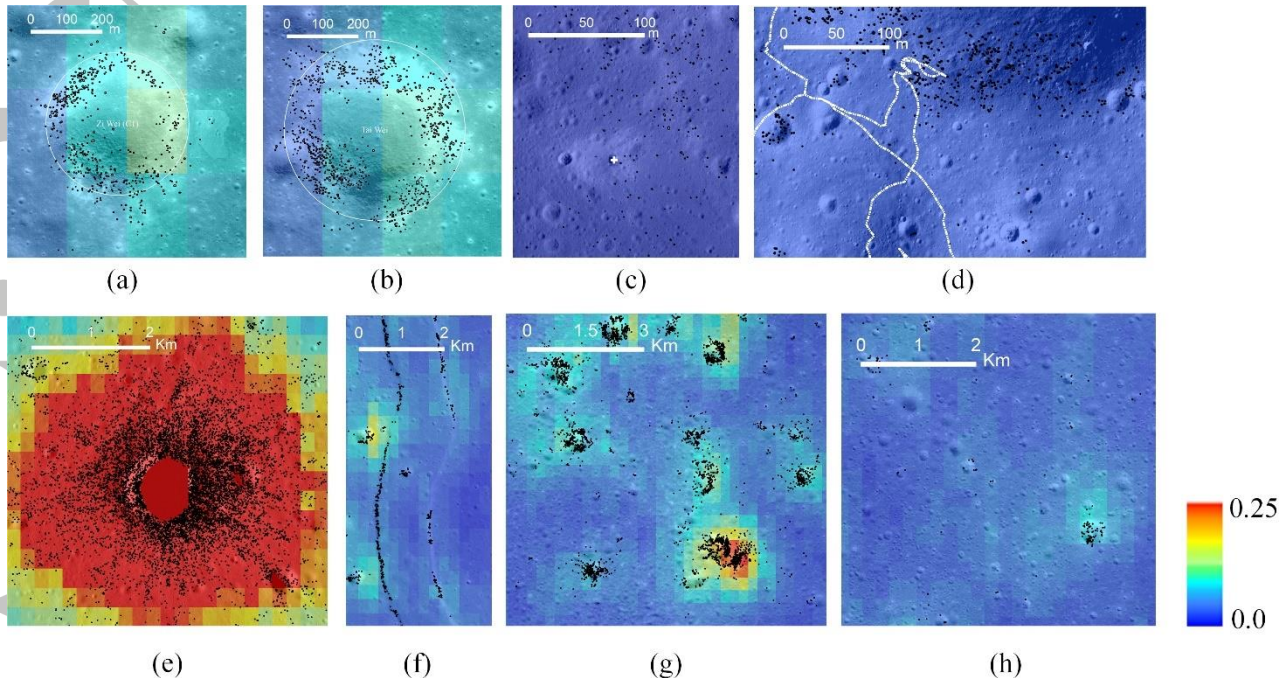


Figure 16. Diviner rock abundance map (128 pixel/degree) overlaid on our rock detection results (marked with black ellipses). (a) The Zi Wei (C1) crater area containing 12 Diviner bins, (b) the Tai Wei crater area containing 12 Diviner bins, (c) the Luna 23 landing area containing 1 Diviner bin, (d) the Luna 17 landing site area containing 2 Diviner bins, and (e)-(h) regions 1-4 in the Oceanus Procellarum area containing hundreds of Diviner bins. The value of each Diviner bin ranges between 0.0 and 0.25 and is color-coded with blue gradually changing to red.

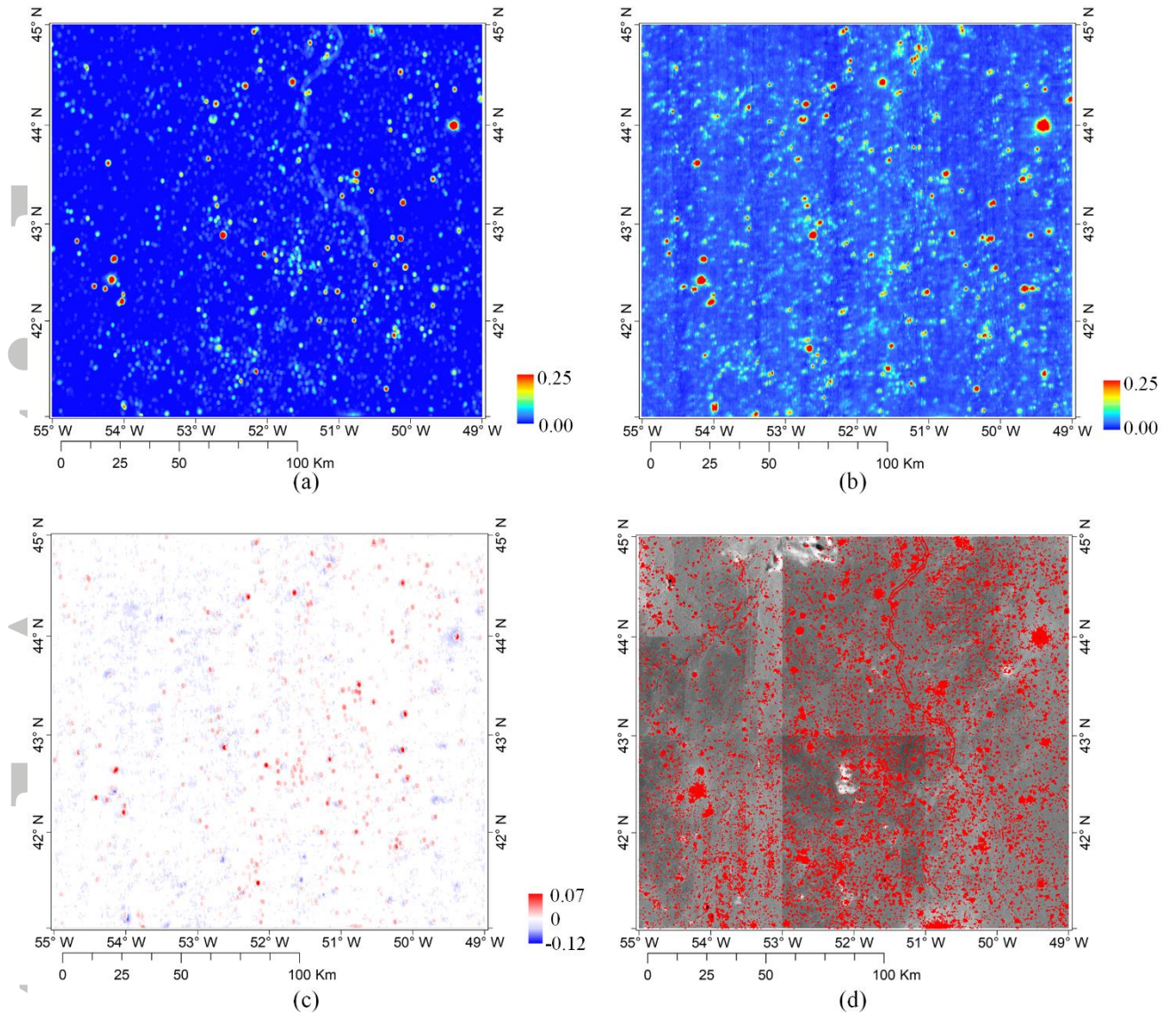


Figure 17. Comparison between the rock abundance maps derived from LRO NAC image mosaic and the Diviner data in the Oceanus Procellarum area, while both of them used the same geographic coordinate system (GCS_MOON_2000) and the same map projection (Mercator). (a) The areal fraction of rocks larger than 1 m estimated using the proposed rock abundance model, (b) the Diviner rock abundance map in the same area, and (c) the difference map generated by (a) minus (b). The red regions denote that the rock areal fraction of our result is greater than that of the Diviner result, and the blue regions represent a less than relationship. (d) The distribution of rocks larger than 3 m in diameter detected from the LRO NAC image mosaic with a resolution of 1.5 m/pixel.

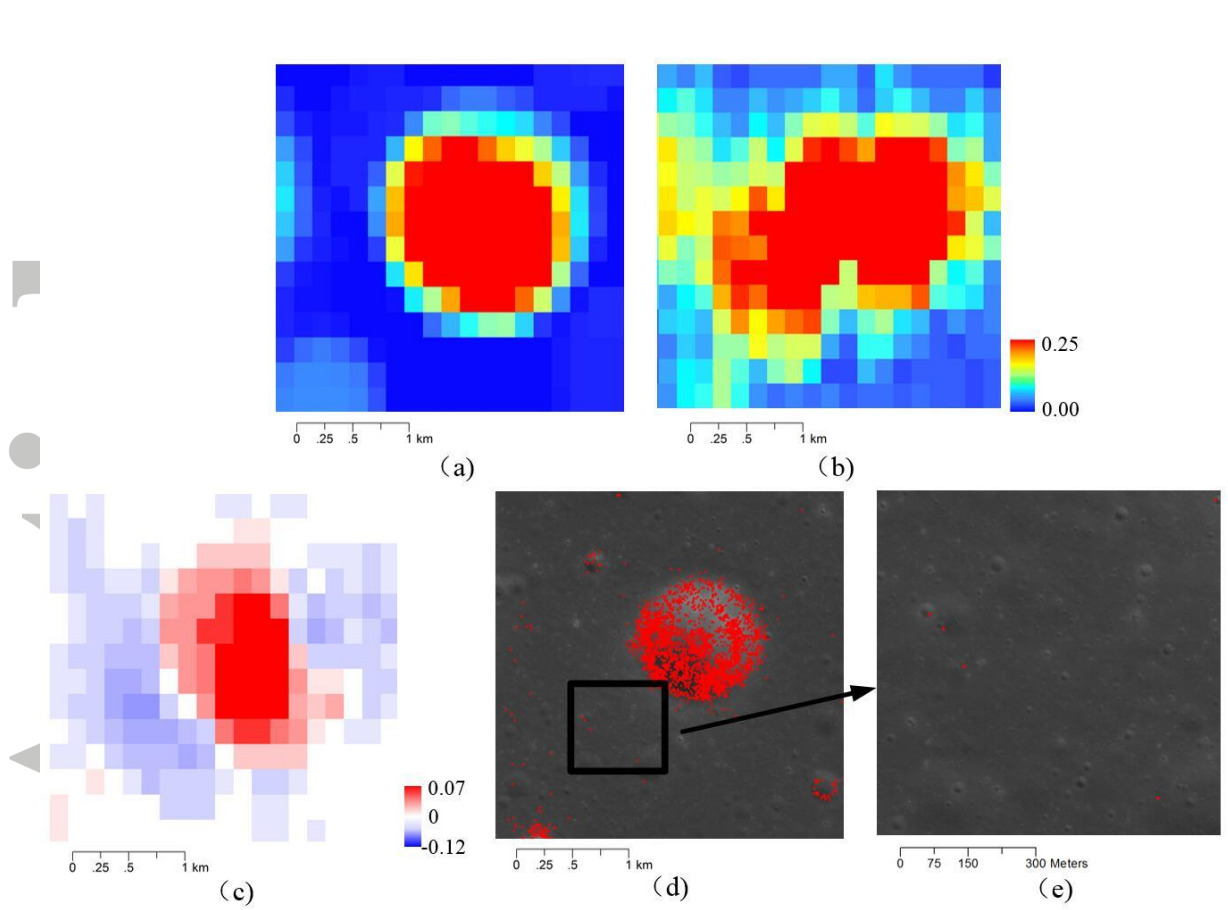


Figure 18. Rock abundance differences around a crater with a diameter of approximately 1.3 km. (a) Rock area fraction estimated by our rock abundance model, (b) rock area fraction derived from Diviner data, (c) differences around the crater, (d) detected rocks overlaid on the LRO NAC image, and (e) a zoomed-in view of the region marked with a box.

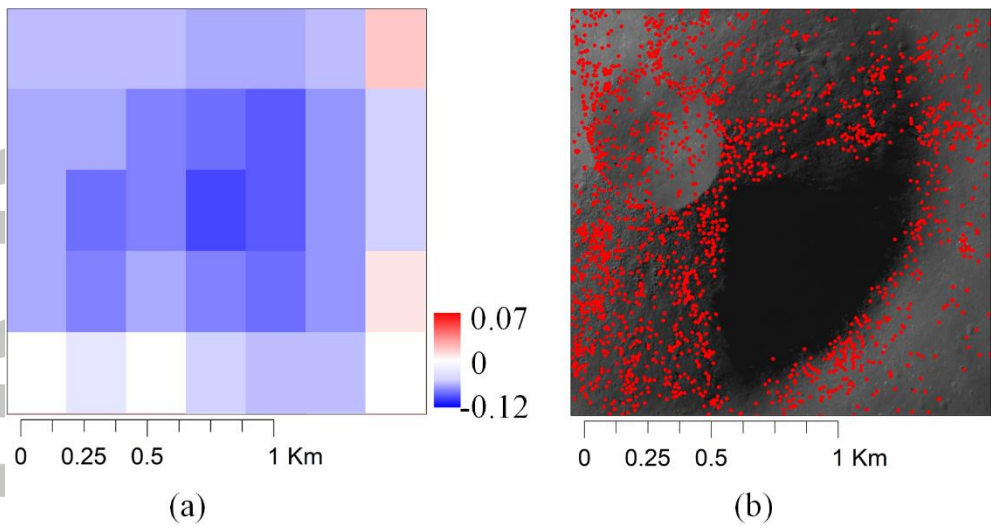


Figure 19. Example of the underestimated rock areal fraction due to shadows in the image.

(a) The difference rock abundance map of a part of a crater, and (b) the detected rocks in the corresponding LRO NAC image.

Accepted

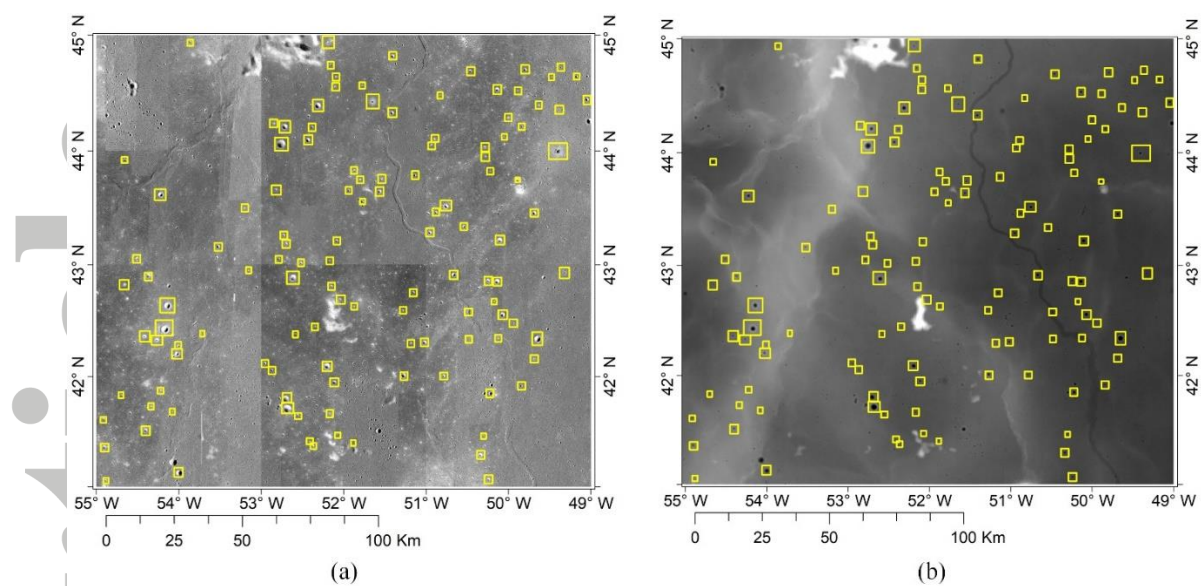


Figure 20. 121 impact craters marked with yellow rectangles distributed in the Oceanus Procellarum study area. (a) 1.5 m/pixel LRO NAC image mosaic, and (b) the 60 m/pixel SLDEM.

Accepted

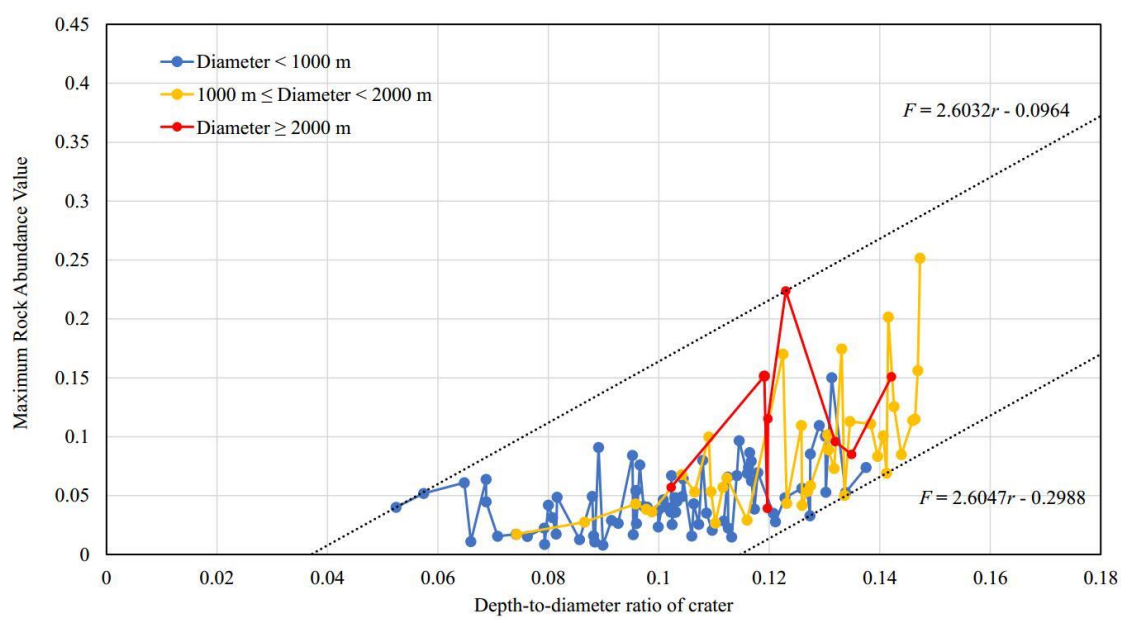


Figure 21. Maximum rock abundance values versus the depth-to-diameter ratio of impact craters.

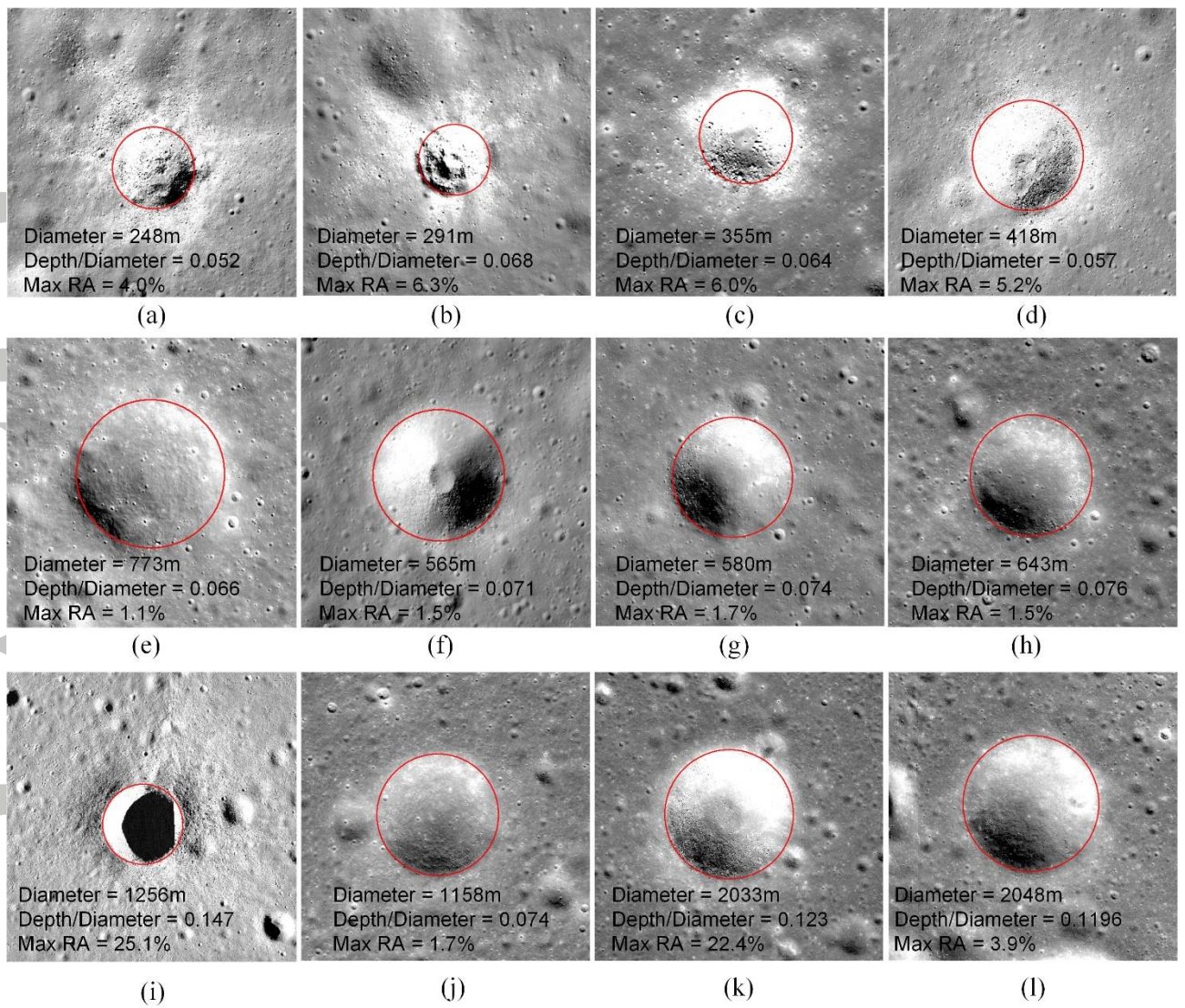


Figure 22. Craters with different depth-to-diameter ratio and rock abundance value. (a) – (d) small craters (≤ 500 m in diameter) with high rock abundance value showing bright crater rays, (e) – (h) craters (≤ 1 km in diameter) with similar depth-to-diameter ratio but unnoticeable crater rays, (i) – (j) craters with the maximum and minimum rock abundance values with diameters in 1–2 km, and (k) – (l) craters with the maximum and minimum rock abundance values with diameters ≥ 2 km.